



HAL
open science

Taking Titan's Boreal Pole Temperature: Evidence for Evaporative Cooling in Ligeia Mare

Robin Sultana, Alice Le Gall, T Tokano, Léa Bonnefoy, Maélie Coutelier, R D
Lorenz

► **To cite this version:**

Robin Sultana, Alice Le Gall, T Tokano, Léa Bonnefoy, Maélie Coutelier, et al.. Taking Titan's Boreal Pole Temperature: Evidence for Evaporative Cooling in Ligeia Mare. *The Astrophysical Journal*, 2024, 961, pp.191. 10.3847/1538-4357/ad0466 . insu-04428397

HAL Id: insu-04428397

<https://insu.hal.science/insu-04428397v1>





Submitted on 31 Jan 2024

HAL is a multi-disciplinary open access archive for the deposit and dissemination of scientific research documents, whether they are published or not. The documents may come from teaching and research institutions in France or abroad, or from public or private research centers.

L'archive ouverte pluridisciplinaire **HAL**, est destinée au dépôt et à la diffusion de documents scientifiques de niveau recherche, publiés ou non, émanant des établissements d'enseignement et de recherche français ou étrangers, des laboratoires publics ou privés.



Taking Titan's Boreal Pole Temperature: Evidence for Evaporative Cooling in Ligeia Mare

R. E. Sultana¹ , A. Le Gall^{1,2}, T. Tokano³ , L. E. Bonnefoy⁴ , M. Coutelier¹, and R. D. Lorenz⁵ 

¹ Laboratoire ATMosphères Observations Spatiales (LATMOS), Université Versailles Saint-Quentin/Université Paris-Saclay, Guyancourt, France

² Institut Universitaire de France (IUF), Paris, France

³ Institut für Geophysik und Meteorologie, Universität zu Köln, Köln, Germany

⁴ Laboratoire d'Etudes du Rayonnement et de la Matière en Astrophysique, Observatoire de Paris, Paris, France

⁵ Johns Hopkins Applied Physics Laboratory, 1100 Johns Hopkins Road, Laurel, MD, USA

Received 2023 June 29; revised 2023 October 10; accepted 2023 October 16; published 2024 January 25

Abstract

From 2004 to 2017, the Cassini RADAR recorded the 2.2 cm thermal emission from Titan's surface in its passive (radiometry) mode of operation. We use this data set to investigate the seasonal evolution of the effective temperature sensed by the microwave radiometer in two regions in the northern pole of the satellite: the sea Ligeia Mare, and its nearby solid terrains. We find that despite the arrival of summer at the end of the mission, the effective temperature of Ligeia Mare decreased by almost 1 K, while that of the solid region slowly increased until 2017 by 1.4 ± 0.3 K. These observations, as well as the lag in summer warming observed by Cassini's Composite Infrared Spectrometer, can be explained by evaporative cooling in both the solid and liquid surfaces after the vernal equinox. It therefore supports the idea that the northern polar terrains are wet. Using an ocean circulation model, we show that the cooling of the sea surface should initiate convection in the sea's interior, ultimately cooling the whole liquid column sensed by the Cassini radiometer and thus decreasing the temperature at depths even long after the evaporation period has ceased. Overall, this work highlights the key role of methane hydrology in controlling the surface and submarine temperatures in the boreal polar regions of Titan.

Unified Astronomy Thesaurus concepts: Titan (2186); Radar observations (2287); Effective temperature (449); Brightness temperature (182); Astronomy data analysis (1858); Planetary polar regions (1251)

1. Introduction

Saturn's moon Titan is the only natural satellite surrounded by a dense and dynamic atmosphere (Kuiper 1944). The presence of this atmosphere, associated with a methane cycle (Lunine & Atreya 2008), has resulted in the formation of Earth-like landscapes at the surface of Titan. Indeed, piercing through the opaque atmosphere, the Cassini-Huygens mission (2004–2017) revealed dune fields (e.g., Lorenz et al. 2006), karstic canyons (e.g., Malaska et al. 2020), river channels (Lorenz et al. 2008), and lakes and seas of liquid hydrocarbons (e.g., Stofan et al. 2007). All of Titan's observed lakes and seas are polar, and they are mostly located in the boreal (north) pole.

Like Earth, Titan experiences seasons, which last about 7.5 Earth years (a cronian year lasts 29.5 Earth years). The Cassini mission thus spanned two Titan seasons: it arrived at Saturn in 2004 just after the northern winter solstice, and it ended a few months after the northern summer solstice, which occurred in 2017 May. Its latest extension, called the Solstice mission, started after the vernal Equinox in 2009 August (i.e., the beginning of spring in the northern hemisphere). One of the main objectives of the Solstice mission was to monitor changing seasons in the Saturnian system, in particular, by searching for surface and atmospheric changes in Titan's polar regions, where the seasonal effects are expected to be most pronounced. Possible windblown waves on lakes (Barnes et al. 2011; Hofgartner 2014) as well as evidence of rainfall events (Dhingra et al. 2019) were detected in the northern polar

regions, especially at the end of the mission as solar heating was increasing and winds peaked. Cassini also recorded the global migration of clouds from the southern to the northern hemisphere, thus tracking solar heating (Turtle 2018). Herein, we investigate the seasonal variations in Titan's surface temperature in and near the polar liquid expanses.

To first order, the physical temperature of Titan's surface can be estimated as nearly constant in both time and space (Flasar et al. 1981; Courtin & Kim 2002). Due to the low incident solar flux reaching its surface (1/1000 of what Earth receives) and the high thermal inertia of its atmosphere, diurnal and seasonal (including latitudinal) variations in the surface temperature are limited, as is the effect of surface albedo (Lorenz 1999). Voyager 1 radio-occultation measurements indeed show no diurnal effect and point to lapse rates in the lower atmosphere lower than 1.5 K km^{-1} (McKay 1991). Voyager infrared observations indicate a pole-to-equator temperature contrast of 2–3 K (Flasar et al. 1981; Flasar 1998).

The Cassini mission somewhat confirmed these predictions and first measurements. Onboard the Cassini spacecraft, two instruments were able to measure the physical temperature of Titan's surface: the Cassini Composite InfraRed Spectrometer (CIRS) through a spectral window of low opacity in the thermal IR (Brown et al. 2004; Sotin et al. 2005), and the Cassini RADAR, which is used as a (passive) microwave radiometer (Elachi et al. 2005; Janssen et al. 2009, 2016). Both instruments monitored the surface brightness temperature at their respective wavelengths (19 μm and 2.2 cm, respectively) during almost two Titan seasons. It is important that these two instruments probed different depths: the very surface for CIRS, and decimeters above land to tens of meters in liquids for the

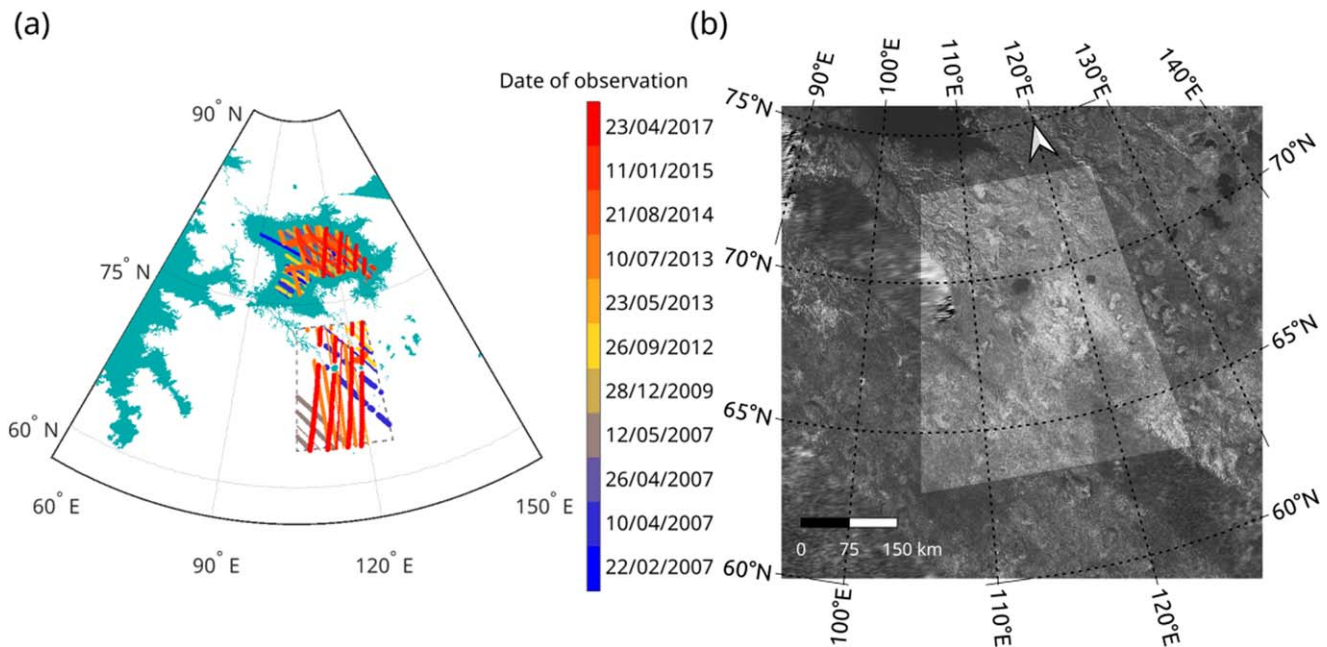


Figure 1. (a) Portion of the boreal polar region centered on Ligeia Mare (seas and lakes are plotted in turquoise) and the solid terrains of interest (inside the dashed gray frame). All flybys over the RoIs are represented with a color-code indicating their respective observation date. (b) Cassini SAR mosaic of the solid RoI.

microwave radiometer (Mastrogiuseppe et al. 2014; Janssen et al. 2016; Le Gall et al. 2016).

From the analysis of the CIRS data set, Cottini et al. (2012) reported the detection of a diurnal signal over the lands in tropical regions of 1–1.5 K, which is indicative of a thermal inertia of 300–600 MKS according to atmospheric models (Tokano 2005). Meanwhile, Jennings et al. (2009, 2016, 2019) found a 2–4 K equator-to-pole difference and noted a delay in the northern warming at the end of the mission, as summer was on its way. This was later interpreted as a cooling effect of both the lakes and the surrounding moist lands because CIRS observations showed no difference in the thermal behavior of these two types of terrains (within a measurement uncertainty of about 0.5 K and based on measurements that barely resolved the seas).

From the radiometry data set, Janssen et al. (2016) found latitude-dependent seasonal temperature variations smaller than those measured by CIRS by a factor of 0.94 ± 0.05 in relative amplitude, which is consistent with a penetration depth of 40 cm to 1 m in organic (dry or wet) sands. The difference with CIRS observations is slightly more pronounced in the northern hemisphere, likely owing to the presence of lakes and seas in which microwaves penetrate deeper than in dry lands. In the north pole, Le Gall et al. (2016) also reported the hint of a slower than expected rise in temperature in the second largest sea of Titan, Ligeia Mare, toward the end of the mission. Diurnal effects are negligible, based on observations (Janssen et al. 2016), which is consistent with the expectation that the radiometer probes much deeper depths than the diurnal skin depth (Lorenz et al. 2003).

This work investigates the temporal variations in Titan’s surface temperature further using the full Cassini microwave radiometry data set. Now that the Cassini mission has ended, we present an analysis of all high- and low-resolution radiometry observations recorded in the boreal polar region (at latitudes higher than 63°N). We especially focus on Ligeia Mare and its surrounding solid lands to expand upon the work

of Le Gall et al. (2016) and to further investigate the lag in summer warming observed in Titan’s high northern latitudes by both CIRS and the Cassini radiometer. Measurements over the sea are compared to an ocean circulation model (Tokano & Lorenz 2016), providing clues on the role of precipitation and evaporation in temperature variations with time.

2. Cassini Radiometry Observations of the Boreal Pole

Between 2004 and 2017, the Cassini spacecraft performed 127 flybys of Titan. Active (or radar) and passive (or radiometry) measurements were collected with the Cassini RADAR during about half of these flybys. Herein, we focus on passive microwave radiometry observations, which recorded the thermal emission from Titan’s near-subsurface at 2.2 cm wavelength in the form of antenna temperatures.

A total of 118 distant unresolved (i.e., disk-integrated) radiometry observations were performed at Titan, covering all latitudes and epochs. A subset of these observations was reduced and analyzed for the first time by Janssen et al. (2009), providing some insight into seasonal variations in temperature. These data are discussed in the Appendix in Section A.1, and in particular, those acquired with a subspacecraft point within the polar circles (12 in the boreal and 5 in the austral pole) are presented in the Appendix in Figure A5 (Section A.5). Although the time sampling is relatively low, these unresolved observations of the polar regions indicate seasonal variations consistent with the expected rise in the temperature during the boreal spring, and a drop during the austral fall.

Resolved microwave radiometry was acquired locally with varying spatial resolution and at various epochs (Janssen et al. 2016). We identified two regions of interest (RoIs) in the boreal pole that were observed at several instances over the course of the Cassini mission. (i) The liquid RoI: Ligeia Mare ($126,000 \text{ km}^2$) was observed on 10 occasions with a spatial resolution of about a few dozen kilometers per footprint, and (ii) the solid RoI: some solid terrains south of Ligeia Mare (between 63° and 73°N and 105° and 125°E —an area of size $335 \text{ km} \times 449 \text{ km}$, Figure 1(b))

Table 1
Characteristics of the Cassini Radiometry Flybys over Ligeia Mare and the Solid RoI

Flyby	Date (yy/mm/dd)	L_s (deg) ^a	Range of Footprint Dimensions $b \times a$		$T_b^{2.2\text{cm}}$ (K) at Normal Incidence and Equinox		$T_{\text{eff}}^{2.2\text{cm}}$ (K) at Normal Incidence	
			(km \times km)					
			Ligeia Mare	Solid Terrains	Ligeia Mare	Solid Terrains	Ligeia Mare	Solid Terrains
T25	07/02/22	331	(26–34) \times (26–136)	...	89.50 \pm 0.9	...	90.66 \pm 0.9	...
T28	07/04/10	333	(15–19) \times (15–79)	(18–24) \times (18–108)	90.5 \pm 0.8	87.01 \pm 0.9	91.71 \pm 0.8	90.8 \pm 1.0
T29	07/04/26	334	(12–15) \times (12–75)	...	90.23 \pm 0.8	...	91.44 \pm 0.9	...
T30	07/05/12	335	...	(15–17) \times (15–75)	...	87.87 \pm 1.1	...	92.3 \pm 1.1
T64 ^b	09/12/28	4	(7–9) \times (7–46)	...	89.81 \pm 0.8	...	91.48 \pm 0.8	...
T86	12/09/26	37	(9–10) \times (9–52)	(8–9) \times (7–47)	89.35 \pm 0.8	87.24 \pm 0.9	91.38 \pm 0.9	94.1 \pm 0.9
T91	13/05/23	42	(10–12) \times (10–12)	(7–9) \times (7–9)	88.61 \pm 0.9	87.74 \pm 1.3	90.73 \pm 0.9	91. \pm 1.3
T92	13/07/10	43.5	(12–17) \times (12–77)	(10–12) \times (9–60)	90.07 \pm 0.9	87.57 \pm 1.1	92.22 \pm 1.0	91.6 \pm 1.2
T104	14/08/21	59	(23–27) \times (23–113)	(33–34) \times (143–150)	88.342 \pm 0.8	87.45 \pm 0.8	90.59 \pm 0.8	91.2 \pm 0.8
T108	15/01/11	63	(9–11) \times (9–48)	...	88.19 \pm 0.8	...	90.47 \pm 0.9	...
T126	17/04/23	89	(11–13) \times (11–64)	(13–20) \times (14–93)	88.39 \pm 0.8	87.50 \pm 1.0	90.86 \pm 0.8	91.6 \pm 1.0

Notes.

^a L_s is the solar longitude. $L_s = 0^\circ$ corresponds to the vernal equinox.

^b On 2009 December 29, a Cassini downlink to the antenna complex in Madrid, Spain, was significantly affected by heavy rain. Seventy-six minutes of telemetry were lost due to both rain and an incorrect set of parameters used for the receiver (downlink controller table). Even though a second redundant playback of the spacecraft solid-state recorder was planned and executed, the redundant playback was in the same pass and was also affected. As a result, data from Titan Pass T64 were very noisy (see Figures A4–B1 in the Appendix). Uncertainties are computed as the square root of the quadratic sum of the radiometer precision and the standard deviation of the derived temperature within an observation (see Section 4.1).

were observed 7 times. SAR images (Figure 1b) show that this region consists of plains sprinkled with a few (mainly empty) small lakes (Barnes et al. 2011), hummocky terrains (Lopes et al. 2020), and rivers channels (in particular, Kokytos and Vid Fluminae). It probably also includes networks of channels with sizes smaller than the SAR resolution (300 m at best). For this work, we focus on these two RoIs because they benefit from the best temporal and spatial sampling by the Cassini radiometer, as reported in Table 1 and illustrated by Figure 1. More details of the investigated observations are given in the Appendix in Table B1 and in Figure B1 (Section A2.1).

The radiometry observations acquired by the Cassini RADAR were calibrated accounting for gain variation over time, antenna pattern sidelobes, and atmospheric opacity, and were converted into brightness temperature ($T_b^{2.2\text{cm}}$) as described in Janssen et al. (2016). The radiometer gain is time-dependent on two timescales. The short-term variations are mainly due to power-supply voltages and environmental temperature variations and are corrected as explained in Janssen et al. (2009). The long-term drift with time (on a yearly timescale) is mainly due to the aging of amplifier components. It can be assumed to be linear and was first determined based on observations of Saturn acquired between 2005 and 2010 (Janssen et al. 2013) and then adjusted iteratively using all Titan radiometry data sets to minimize the residuals in overlapping data (Janssen et al. 2016). It was estimated to be $-0.22\% \text{ yr}^{-1}$. Note that because of the way it is determined, the resulting value of the radiometer gain long-term drift also accounts for the variation in Saturn’s distance to the Sun during the mission (from 9.06 au in 2004 October to 10.04 au in 2017 September).

In the calibration and map-making process, the brightness temperatures are also corrected to a common viewing geometry (namely normal incidence angle) and to a common epoch (namely Saturn’s vernal Equinox, i.e., 2009.61;

Janssen et al. 2016). This later correction can be removed by inverting Equation (1). More specifically, the brightness temperatures measured at a given epoch t counted from the equinox (2009.61) and at a latitude δ are corrected to the Equinox (t_{Eq}) epoch as follows:

$$T_b^{2.2\text{cm}}(\delta, t_{\text{Eq}}) = T_b^{2.2\text{cm}}(\delta, t) \times \frac{T_{\text{eff}}^{J2016}(\delta, t_{\text{Eq}})}{T_{\text{eff}}^{J2016}(\delta, t)}, \quad (1)$$

with

$$T_{\text{eff}}^{J2016}(\delta, t) = T_{S,\text{IR}}(\delta, t_{\text{Eq}}) + F_{2\text{cm}}[T_{S,\text{IR}}(\delta, t) - T_{S,\text{IR}}(\delta, t_{\text{Eq}})], \quad (2)$$

where $T_{S,\text{IR}}(\delta, t)$ is the updated version of the empirical surface temperature model proposed in Jennings et al. (2016) derived from CIRS observations at $19 \mu\text{m}$ (D. Jennings, personal communication), namely

$$T_{S,\text{IR}}(\delta, t) = (93.53 - 0.08t) \cos(0.0029(\delta + (3.3 - 3.9t))). \quad (3)$$

The term $F_{2\text{cm}}$ represents the attenuation of the temperature variations at the depths sensed by the radiometer, and is set to 0.94 (updated from Janssen et al. 2016 in 2018 as it presents the optimum value for the temperature variation attenuation in the subsurface). The resulting $T_b^{2.2\text{cm}}$ are accurate to $<2\%$ with a precision of 0.8% (Janssen et al. 2016).

In Table 1 the brightness temperatures averaged over each RoI are corrected to normal incidence and to the equinox epoch, and only the values measured with a radiometry footprint that lies to 99% at least within the (liquid or solid) RoI are kept (Figure 1(a)). For Ligeia Mare, the RoI is slightly smaller than the sea in order to remove residual contribution from shores, if any (a conservative margin of 20 km is taken, which typically corresponds to four radiometry footprints). Moreover, footprints including islands are not taken into account. In total, there are between 50 (T28) and 341 (T108)

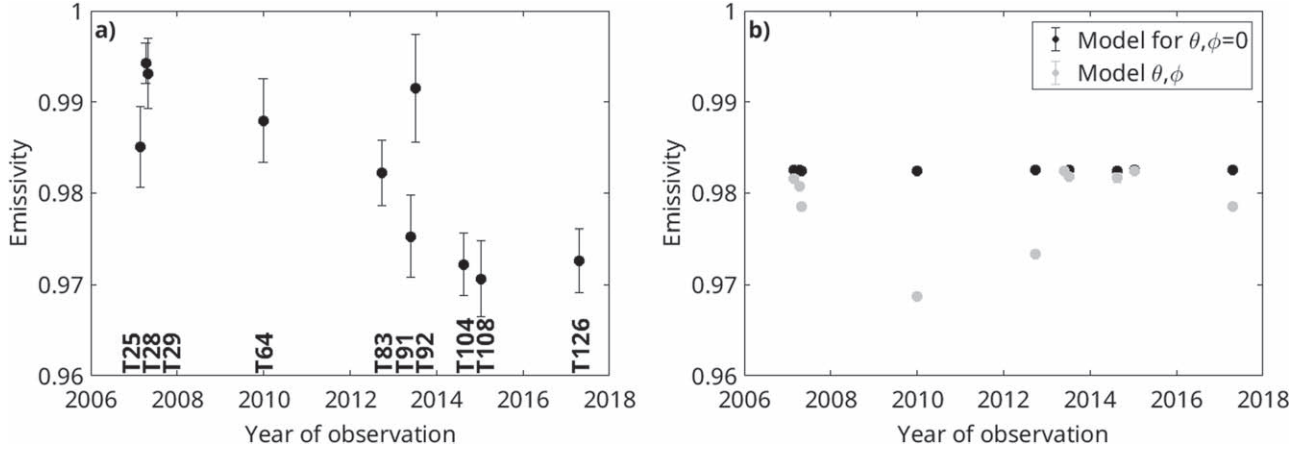


Figure 2. (a) Temporal variations of the emissivity of Ligeia Mare derived from dividing the measured brightness temperatures (corrected to normal incidence and equinox) by $T_{\text{eff}}^{J2016}(\delta, t_{\text{Eq}})$. (b) Expected variations in the emissivity of Ligeia Mare from one flyby to the next, assuming no change in composition and taking into account the bathymetry of the sea at normal incidence (black) and accounting for the different geometry of observations of each flyby (gray).

radiometry observations over Ligeia Mare per flyby and between 39 (T104) and 618 (T92) over the solid RoI.

3. Derived and Modeled Emissivity over Ligeia Mare

In the microwave domain, the Rayleigh–Jeans approximation applies, and the recorded $T_b^{2.2\text{cm}}$ are simply the product of the near-subsurface emissivity at 2.2 cm (e) and the surface physical effective temperature $T_{\text{eff}}^{2.2\text{cm}}$, thus

$$T_b^{2.2\text{cm}} = eT_{\text{eff}}^{2.2\text{cm}}. \quad (4)$$

We recall that because microwaves can probe much greater depths than infrared wavelengths, they are not only sensitive to the surface temperature, but to a physical effective temperature $T_{\text{eff}}^{2.2\text{cm}}$ that corresponds to the temperature profile weighted by a radiative transfer function and integrated over depth. In the case of Ligeia Mare, the Cassini RADAR/radiometer actually probed the entire liquid column due to the extreme transparency of liquid methane to microwaves (Mastrogiuseppe et al. 2014; Mitchell et al. 2015; Le Gall et al. 2016).

3.1. Measurement-derived Emissivity over Ligeia Mare

The emissivity shown in Figure 2(a) is obtained by dividing the $T_b^{2.2\text{cm}}(\delta, t_{\text{Eq}})$ measured over Ligeia Mare (given in Table 1) by the effective temperature modeled at equinox, $T_{\text{eff}}^{J2016}(\delta, t_{\text{Eq}})$ (Equation (2)). It should provide a good estimate of the emissivity (corrected to normal incidence) of the sea. However, Figure 2(a) shows unexpected variations (namely a general decrease) with time that is in line with preliminary observations investigated in Le Gall et al. (2016). It is indeed unlikely that the emissivity of the whole sea would significantly change with season as it would imply a global and dramatic change in the liquid composition in a few years, that is, a change in the dielectric constant of a volume estimated to be 14,000 km³ (Hayes 2016). Instead, the apparent decrease in emissivity in Figure 2(a) is most likely due to an overcorrection for the seasonal effect owing to an overestimation of $T_{\text{eff}}^{J2016}(\delta, t)$ at the end of the mission (Equation (1)). This hypothesis is further investigated in Section 4.

Nevertheless, our data set being limited (10 flybys) and heterogeneous (in terms of resolution, of the geometry of observation, and of the covered area; see also Figure B1), to

confirm this hypothesis, we compare the derived emissivity values to modeled values obtained accounting for the different location of the flyby ground track and the bathymetry of Ligeia Mare. In the section below, we also investigate the effect of an incorrect correction for the geometry of observation.

3.2. Model for the Emissivity

The microwave emissivity of a terrain depends on its composition, density, and subsurface heterogeneity, and, to a lesser extent, on its surface roughness. In absence of much information on the solid terrains of interest, their emissivity is estimated under the assumption that they are smooth, with a homogeneous subsurface with a permittivity of ε_S . Accounting for the viewing geometry (characterized by the incidence or emission angle θ and the polarization angle φ), the emissivity can be estimated as follows (Heiles & Drake 1963):

$$e = e_{\perp}(\varepsilon_S, \theta) \cos^2(\varphi) + e_{\parallel}(\varepsilon_S, \theta) \sin^2(\varphi), \quad (5)$$

where e_{\perp} and e_{\parallel} are the emissivities in perpendicular and parallel polarizations, respectively, derived from the Fresnel reflection coefficients as $e_p = 1 - \Gamma_p$ for a given polarization p (see, e.g., Equation (6.88a) and (6.88b) of Ulaby & Long 2015).

In the case of a hydrocarbon lake, the emissivity depends on the liquid composition, surface, and seafloor roughness, but also on the bathymetry and seafloor composition. All these characteristics are relatively well known for Ligeia Mare, which is the first extraterrestrial sea for which a depth profile was made available (Mastrogiuseppe et al. 2014). Cassini RADAR altimetry observations of this sea compared to laboratory measurements of the cryogenic liquid alkane microwave absorptivity (Mitchell et al. 2015; Mastrogiuseppe et al. 2016) indeed demonstrate that Ligeia Mare is likely composed of the following ternary mixture: 71% CH₄, 12% C₂H₆, and 17% N₂. This liquid composition is especially transparent to microwaves with a loss tangent $\tan \Delta$ of $(4.4 \pm 0.9) \times 10^{-5}$ (inferred from RADAR altimetry observations; Mastrogiuseppe et al. 2016) and a bulk permittivity of $\varepsilon_L = 1.7 \pm 0.02$ (computed with the values of permittivity measured by Mitchell et al. 2015 for CH₄ and C₂H₆, and by Paillou et al. 2008 for N₂ and using the Lorenz-Lorenz mixing law). The electrical skin depth at $\lambda = 2.2$ cm $\delta_{el} \approx \frac{\lambda}{\sqrt{\varepsilon'_L \tan \Delta}}$ in Ligeia Mare—a proxy for the sounding depth of the radiometer

—is as high as 61 m, which is almost 3000 times the wavelength. The Cassini radiometer therefore sensed the whole liquid column, including the seafloor, whose permittivity was here set to $\varepsilon_{\text{SF}} = 2.25$, in agreement with Le Gall et al. (2016; who found $\varepsilon_{\text{SF}} < 2.9 \pm 0.9$) and Zebker et al. (2014; who found that the permittivity of the shores of Ligeia Mare is between 2.2 and 2.3).

Further, assuming no scattering inside the liquid layer and a smooth sea surface and seafloor, the emissivity of Ligeia Mare is estimated using the two-layer model proposed by Le Gall et al. (2016), which consists of applying Equation (5), with for a given polarization p (\perp or \parallel),

$$e_p = \frac{1 - \Gamma_{p1}}{1 - \Gamma_{p1}\Gamma_{p2}L_1^2}((1 + \Gamma_{p2}L_1)(1 - L_1) + (1 - \Gamma_{p2})L_1), \quad (6)$$

where $\Gamma_{p1}(\varepsilon_L, \theta)$ and $\Gamma_{p2}(\varepsilon_L, \varepsilon_{\text{SF}}, \theta)$ are the Fresnel reflection coefficients at the interfaces air/sea and sea/seafloor, respectively, and $L_1 = e^{-\frac{d}{\varepsilon_L \cos \theta'}}$ is the power attenuation (due to absorption) in a liquid layer of thickness d . At a given location (i.e., for a given radiometry measurement/footprint), d is known from the best available bathymetry map of Ligeia Mare (published in Hayes 2016). $\theta' = \sin^{-1}\left(\sin \frac{\theta}{\sqrt{\varepsilon_L}}\right)$ is the transmitted angle in the liquid.

Figure 2(b) presents the modeled emissivity values of Ligeia Mare for each flyby both at normal incidence and when the viewing geometry is accounted for. For this latter case, the simulated emissivity variations from one flyby (epoch) to another show absolutely no correlation with the observed variations with time of the emissivity (Figure 2a). In particular, the minimum emissivity is not observed during T64, in contrast to what is predicted by the model. This rules out an incorrect correction of the geometry of observation as a possible explanation for the general decrease in emissivity displayed in Figure 2a. Furthermore, the model shows that the emissivity values at normal incidence should vary barely from one flyby to the next (only small emissivity variations < 0.005 are expected due to the different bathymetry of the probed regions of the sea). Moreover, we checked in Section B.3 that the sea composition does not dramatically change the permittivity and hence the emissivity, and we showed that a large increase in the permittivity (30%) is needed to decrease the emissivity by 2%. This prediction is also supported by active radar (SAR) observations that show no evidence of change in reflectivity of the sea with season (see Figure B3 in the Appendix B). It further implies that the observed variations in emissivity in Figure 2a, and in particular, its general decrease, must be due to an incorrect correction of the seasonal change in the temperature. In other words, the T_{eff}^{J2016} law (Equation (2)) we used does not describe the temporal variations in the physical temperature of the sea well. This is expected because the law in question is mainly based on surface rather than sea observations.

In the following, we therefore assume that the emissivity of Ligeia Mare (as well as that of the solid RoI) remains constant over the course of the Cassini mission and that temporal variations of $T_b^{2,2\text{cm}}$ primarily reflect variations in $T_{\text{eff}}^{2,2\text{cm}}$ with time (Equation (4)). We thus investigate the temporal evolution of the effective temperature of our selected liquid and solid RoIs using all available microwave radiometry data reported in Table 1. Our results are then compared to the CIRS-derived

temperature model and to predictions of an ocean circulation model.

4. Seasonal Variations of the Effective Temperature of Ligeia Mare and Nearby Solid Terrains

4.1. Derived $T_{\text{eff}}^{2,2\text{cm}}$ and Comparison with CIRS Temperatures

Following Equation (4), effective temperatures are derived by dividing each available value of $T_b^{2,2\text{cm}}$ (corrected back to their epoch of acquisition; see Section 2 and Equation (1)) by the value of emissivity modeled at normal incidence for the relevant RoI (Section 3.2). The emissivity of the liquid RoI uses the dielectric constant model detailed in Section 3.2, whereas for the solid RoI, we tested three different dielectric constants of 1.7, 2.3, and 2.7. The resulting $T_{\text{eff}}^{2,2\text{cm}}$ values are then averaged to provide a mean $T_{\text{eff}}^{2,2\text{cm}}$ per flyby as reported in Table 1. The temporal variations of $T_{\text{eff}}^{2,2\text{cm}}$ are presented in Figure 3(a) and 3b for the solid and liquid RoIs, respectively. The error bars are computed as the root square of the quadratic sum of the relative uncertainty on the calibrated $T_b^{2,2\text{cm}}$ (0.8 %) and the standard deviation of the derived $T_{\text{eff}}^{2,2\text{cm}}$ values for a given flyby. These latter are larger for the solid RoI, which includes a variety of terrains. For each flyby, we verified that there was no systematic offset in the whole swath that could be caused by a calibration error. This was done by comparing the effective temperatures extracted over nearby solid terrains in overlapping data acquired during different flybys at the closest possible dates and was especially important for T25 and T92, which are associated with temperatures that are lower by about 1 K (T25) or higher (T92) than the general trend on Ligeia Mare (see more details in Figure B2 in the Appendix B).

In order to estimate the slope (and associated uncertainty) of the temporal variations (assumed to be linear over the course of the Cassini mission) $T_{\text{eff}}^{2,2\text{cm}}$ of both the solid and liquid surfaces, we use a bootstrap Monte Carlo technique that accounts for uncertainties. This technique consists of generating a large number of synthetic data by random sampling with a replacement of values from the observed data at a given epoch and search, at each trial, for the best-fit linear law describing the variations of $T_{\text{eff}}^{2,2\text{cm}}$ with time. The resulting distribution of slopes after bootstrap-testing the sample with one million trials indicates that the effective temperature of Ligeia Mare dropped by 0.7 ± 0.2 K over the course of the Cassini mission (Figure 3c). A similar result (a drop of 0.8 ± 0.2 K; Figure 3c) is found when averaging the effective temperatures of T25 with T28 and T29, and those of T92 with T91, because of their temporal proximity. This is likely a lower limit for the temperature drop because we recall that the radiometry data were corrected for the increase in Saturn's distance to the Sun during the mission (Section 2) and are thus slightly overestimated at the end of the mission. As an additional sanity check, we conducted the same exercise using only the brightness temperature measured within beam 3 of the radiometer, which has the best calibration (see Janssen et al. 2016). This leads to an even more pronounced decrease of 1.0 ± 0.2 K in the observation period (see Figure B6 in the Appendix B). Last, we also ensure that the estimated temperature drop over Ligeia Mare barely varies (by less than 2%), with slightly different assumed values of ε_L ($1.6 < \varepsilon_L < 1.9$) and ε_{SF} ($2 < \varepsilon_{\text{SF}} < 3$) in the model used to estimate the emissivity at normal incidence (Section 3.2).

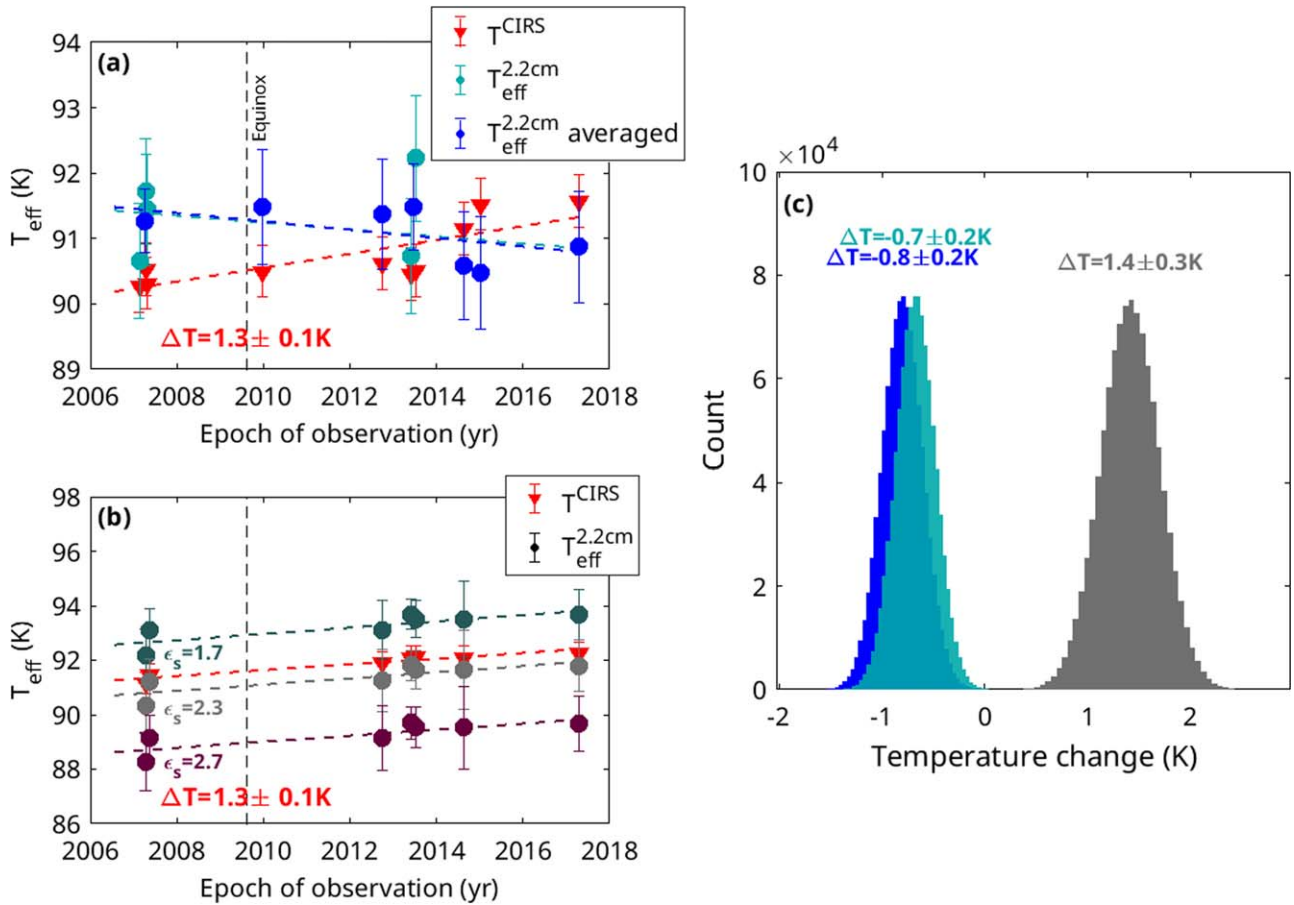


Figure 3. Variations in the 2.2 cm effective temperature $T_{\text{eff}}^{2.2\text{cm}}$ and the surface temperature predicted from the CIRS data T_{CIRS} (Jennings et al. 2019) for the liquid (a) and solid (b) Rols during the Cassini mission. For the solid terrain (b), $T_{\text{eff}}^{2.2\text{cm}}$ is given for different assumed values of the solid-terrain permittivity ϵ_s . (c) Results of the bootstrap Monte Carlo approach displaying the distribution of the change in $T_{\text{eff}}^{2.2\text{cm}}$ during the Cassini mission in the solid (in gray) and liquid (in turquoise) RoIs. The result obtained when averaging T25 measurements with T28 and T29 measurements and T91 measurements with T92 measurements is presented in blue.

This temporal variation differs from the latest model describing surface temperature variations inferred from CIRS measurements at $19\ \mu\text{m}$, which follows the analytical law (Jennings et al. 2019; Figure 3(a))

$$T_{\text{CIRS}}(\delta, t) = (93.53 - 0.095t)\cos((\delta + (0.85 - 3.2t)) \times (0.0029 - 0.00006t)), \quad (7)$$

where t is the time in years measured from Titan equinox (2009.61), and δ is the latitude in degrees. This functional law reproduces the CIRS data set recorded during the whole Cassini mission well, within a rms error of 0.4 K. Equation (7) predicts that T_{CIRS} increases by $1.3 \pm 0.1\text{K}$ over the course of the Cassini mission both at the latitude of the center of Ligeia Mare and at the latitude of the center of the solid RoI (Figures 3(a) and (b)). In contrast, the net difference with the measurements at 2.2 cm suggests that the temperature profile of the whole column of liquid in the sea evolves throughout the year; this is further discussed in Section 4.2.

On the other hand, applying the same method on the solid terrains, we find that $T_{\text{eff}}^{2.2\text{cm}}$ increased by $1.4 \pm 0.3\text{K}$ between 2004 and 2017, regardless of the assumed value of ϵ_s (1.7, 2.3, or 2.7; see Figure 3b), which is very close to the CIRS observations ($1.3 \pm 0.1\text{K}$ based on Equation (7)). We further note that of the three values we tested, $\epsilon_s = 2.3$ provides the best agreement between the CIRS and radiometry absolute temperatures on the solid RoI, which are expected to be close if

the radiometer sounded only the shallow subsurface of the solid RoI.

We recall that CIRS observations have a coarser resolution than the radiometry observations; they do not resolve the seas. Furthermore, they only sense the very surface, whereas the radiometer probes below the air/surface interface, especially in the seas. Jennings et al. (2019) show that CIRS-inferred temperature temporal evolution is well explained by the global circulation model (GCM) developed by Tokano (2019). This GCM includes a simple hydrology (or alkanology) scheme, which predicts the budget of surface methane deposits from precipitation and evaporation. It predicts precipitation in the boreal polar region over the spring season, thus wetting the lands. A consequence of an increase in moisture is an increase in the surface thermal inertia, which delays the surface warming. This GCM better reproduces the delayed and modest increase in the temperatures observed in late spring and early summer than previous predictions that did not account for the hydrology (Jennings et al. 2019).

Although it is different, the derived seasonal evolution of the effective temperature at 2.2 cm, both on Ligeia Mare and the solid lands, supports the idea of the key role of the methane cycle on surface and subsurface temperatures in reducing the summer warming. As an increasing amount of sunlight heats the northern polar terrains, precipitations are more frequent and winds are stronger, which in turn increases the ground thermal

inertia and causes evaporative cooling. At the end of the mission, Cassini indeed captured evidence of rainfall events, e.g., the apparition and subsequent disappearance of methane clouds at polar latitudes (Turtle 2018) and the detection of so-called “bright ephemeral features” between Kraken and Ligeia Maria during the T121 (2016 July 25) flyby (Dhingra et al. 2021). More recently, the James Webb Space Telescope’s Near-Infrared Camera (NIRCam) and images from the ground-based Keck observatory confirmed the presence of extensive methane clouds in the lower atmosphere of the northern pole, which validates predictions that clouds would form readily in the northern hemisphere during its late summertime when the surface is warmed by the Sun. Thus, precipitation and evaporation likely affect both the temperature of Ligeia Mare and of the solid RoI.

Further, we note that T25 and T92 are offset by more than 1 K from the other Ligeia Mare observations. We show in Figure B2 in the Appendix B that these two measurements are not biased because the measured temperatures over solid terrains during these flybys agree well with independent observations in close temporal proximity. The deviation of these two measurements from the general trend may be due to the relatively large uncertainties inherent to radiometry, or they may point to abrupt temporal temperature variations. This latter hypothesis would suggest strong fluctuations of the evaporation rate at these periods that may be related to rapid changes in wind speed at the sea surface, as predicted by Lorenz (2015).

4.2. Predictions from an Ocean Circulation Model: Indication for Convection Induced by Evaporation in Ligeia Mare

Tokano & Lorenz (2016) developed a three-dimensional ocean circulation model for Titan’s seas. This model simulates density-driven circulation that arises due to spatial variations in liquid density when the temperature or methane mole fraction changes in the sea. The sea temperature changes by heat exchange with the atmosphere and heat redistribution within the sea, but heating due to insolation and cooling due to evaporation (latent heat) are the main drivers of temperature variation at the sea surface. The methane mole fraction changes by precipitation and evaporation as well as by transport in the sea. An important mechanism that changes the vertical profile of the temperature and methane mole fraction is convective overturning, which occurs as soon as the vertical density profile becomes unstable (density increase from bottom to top) due to evaporative cooling of the sea surface and decrease in the near-surface methane abundance by evaporation. The imposed precipitation rate at the surface in the ocean circulation model is guided by predictions of GCMs (Tokano 2009; Schneider et al. 2012), but is not directly adopted from the GCMs; it varies with latitude and season. The evaporation rate linearly increases with methane mole fraction at the sea surface, exponentially increases with the sea surface temperature, and entirely ceases if the variable methane vapor pressure over the sea is lower than the atmospheric partial pressure of methane, which was kept constant for simplicity. The dependence of the evaporation rate on the wind speed (ventilation effect) was not taken into account.

The ocean circulation model adapted to the composition of Ligeia Mare was used to predict the temperature profiles in the middle of Ligeia (73°N, 113°E) at the dates of the Cassini radiometry observations (Figure 4(b)). It anticipates a drop in the

temperature at the sea surface after vernal equinox (2009 August) as rainfall begins and evaporation suddenly increases due to increasing methane mole fraction near the sea surface as a result of precipitation (Figure 4(a)). When the sea surface becomes colder than the sea interior and as the methane-to-ethane ratio at the surface decreases due to methane evaporation, the upper cold fluid layer sinks, and the model predicts the onset of a convective overturn. This latter ultimately homogenizes the sea density, thus reducing the temperature at depths, as displayed by the temperature profiles obtained after 2010, in which the sea bottom temperature is 1–2 K colder than before 2010 in Figure 4(b).

Because the Cassini radiometer sounded the entire liquid column of Ligeia Mare, its measurements should have captured this somewhat counterintuitive general cooling effect of both evaporation (at the surface) and subsequent convection (at depth) while summer approaches. We use the predicted temperature profiles $T(z)$ to estimate the effective temperature of the sea (at normal incidence) as follows (see, e.g., Equation (6.89) of Ulaby & Long 2015):

$$T_{\text{eff}}^{\text{OceanModel}} = \frac{\int_0^{+\infty} T(z) e^{-\frac{\sec\theta'z}{\delta_{el}}} dz}{\int_0^{+\infty} e^{-\frac{\sec\theta'z}{\delta_{el}}} dz}. \quad (8)$$

Hence, at normal incidence,

$$T_{\text{eff}}^{\text{OceanModel}} = \frac{\int_0^d T(z) e^{-\frac{z}{\delta_{el}}} dz}{\delta_{el}} + T(d) e^{-\frac{d}{\delta_{el}}}, \quad (9)$$

where z is the depth parameter, d is the sea depth at the location of measurement (known from the bathymetry map of Ligeia Mare; Hayes 2016), and the temperature is assumed to be equal to $T(z=d) = T(d)$ below 100 m or at the sea bottom, where the sea is shallower than 100 m.

Figure 4(c) shows the simulated $T_{\text{eff}}^{\text{OceanModel}}$ as a function of time. Although larger in amplitude with a temperature drop of about 1–1.5 K against 0.7 ± 0.2 K for the observations acquired between 2004 and 2017 (Figure 3c), the simulated effective temperatures follow the same trend as the measurements. The observed temperature drop is thus a further argument for the existence of convection movements in the sea that are triggered by evaporative cooling at its surface. Part of the difference between the measured and simulated effective temperatures could be explained by the fact that Equation (9) neglects the (lower) emission from below the seafloor, if any.

This result would hold true with a more complex ocean circulation model that accounts for wind speed change at the surface. The constant wind speed over the sea that is assumed in the ocean circulation model should have caused some temporal smoothing of evaporative cooling, but it does not affect the timing of the onset and the cessation of evaporative cooling. The sea temperature prediction by Tokano & Lorenz (2016) is also strongly dependent on the light extinction coefficient (turbidity of the sea), which controls the vertical profile of sunlight deposition within the sea. However, the observed temperature variations rule out a very clear sea with a deep penetration of sunlight because in that case, the seasonal variation in sea temperature would be tiny at all depths.

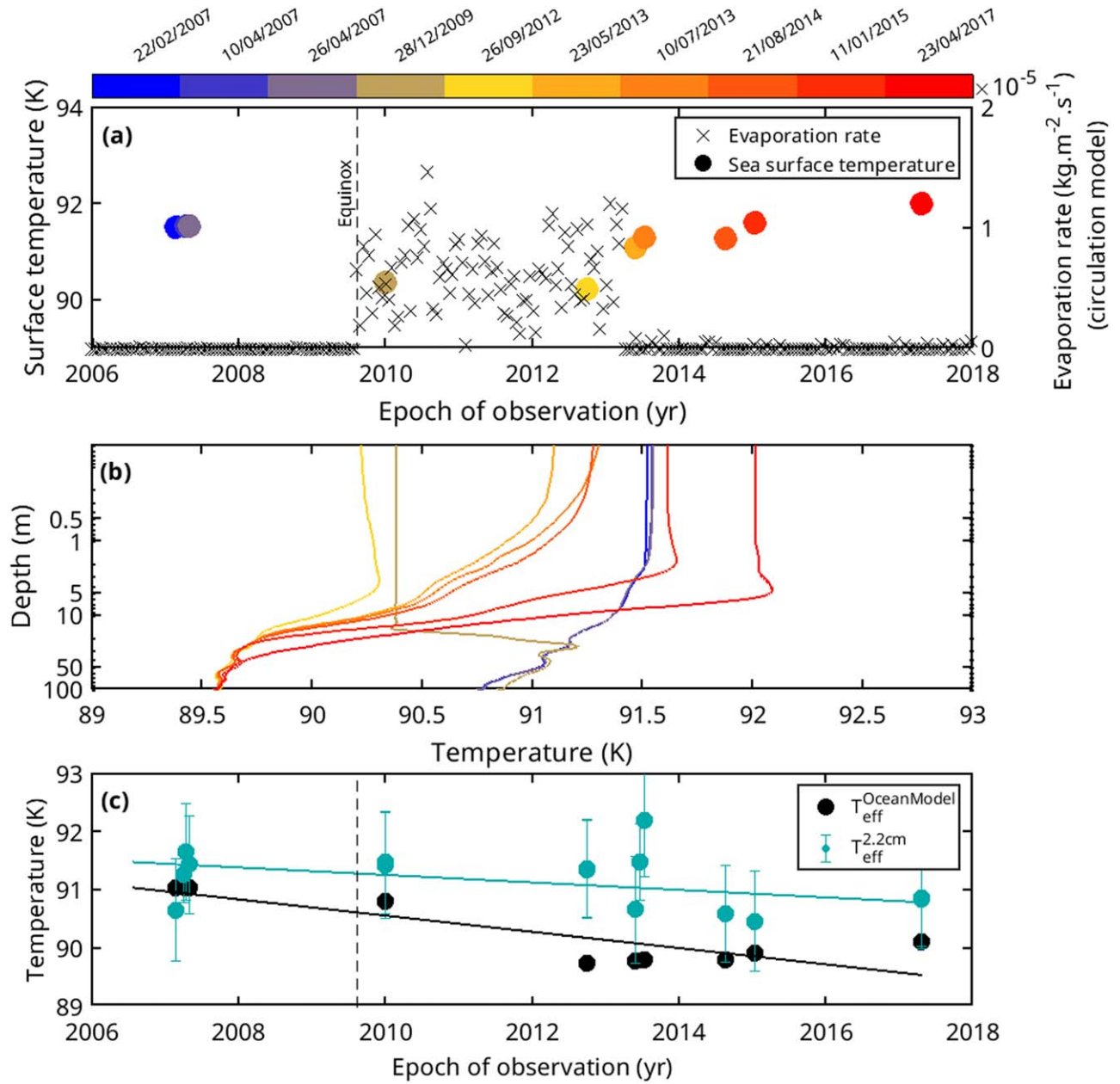


Figure 4. (a) Temperature at the surface of Ligeia Mare at the epochs of the Cassini radiometry observations and concurrent evaporation rate as predicted by the ocean circulation model of Tokano & Lorenz (2016). (b) Simulated temperature profiles in Ligeia Mare at the epochs of the Cassini radiometry observations. The line colors, like the points in (a), correspond to the epoch of observation. (c) Temporal variations in $T_{\text{eff}}^{2.2\text{cm}}$ as recorded over Ligeia Mare (also shown in Figure 3(b)) against the simulated $T_{\text{eff}}^{\text{OceanModel}}$ (see Equation (9)).

5. Conclusion

This work reports seasonal variations in the effective temperature sensed by the Cassini 2.2 cm microwave radiometer in two regions in the boreal pole of Titan, namely Ligeia Mare and the nearby solid terrains. We show that over the 13 years of the Cassini mission, the effective temperature slowly increased, as expected, over the solid terrains, but it decreased in the sea, even though the northern hemisphere went from winter to early summer.

The slowness of the heating of the solid terrains is interpreted as an indication of evaporative cooling, an interpretation that has been advanced before to explain the reduced and delayed summer warming observed by CIRS in the northern pole (Jennings et al. 2019). This further implies

that the solid terrains of the north pole are most likely methane-wet due to precipitation and/or variations in the level of a subsurface alkanifer. It thus supports the idea that methane surface hydrology plays a key role in driving seasonal surface temperatures and has to be included in GCMs.

On Ligeia Mare, we report a minimum decrease in the effective temperature of about 0.7 K (even 1 K considering only beam 3; see Section B.4), consistent with the following scenario: the evaporative cooling of the uppermost layers of the sea after vernal equinox leads to the onset of convection in the sea interior, which ultimately reduces the temperatures at depth. As a consequence, the sea depths are cooler in early summer than in late winter. Comparison with an ocean circulation model confirms that this process can occur in Titan conditions and leads to decreasing temperatures at depth in summer.

Several model hypotheses and approximations can explain the remaining disparity between the observations and the model. In addition to adjusting the evaporation rate to the wind speed, the ocean circulation model could account for temperature differences across the sea. Indeed, we only used the temperature profiles modeled for the middle of Ligeia Mare, while there may exist differences due to exchange processes between the center and the border of the sea. For instance, the temperature difference between the (colder) sea and the (warmer) surrounding lands may generate sea breeze and therefore stronger winds and evaporative cooling at the shores (Chatain et al. 2022).

Unfortunately, no similar investigation could be conducted on other seas, lakes, or solid terrains of the northern pole due to the lack of data that are well sampled in space and time. However, we note that the hint of a similar drop in temperature is observed on Kraken Mare (see Figure B7 in the Appendix B). More data would have been helpful to better constrain the timing of the aforementioned events, and in particular, of evaporation and precipitation on Titan. In this context, an orbiter mission to Titan, flying on a polar orbit as proposed by Rodriguez et al. (2022), would greatly help explore the interactions between the hydrocarbon lakes and the atmosphere through the methane cycle. Meanwhile, there may be opportunities to monitor the evolution of the surface temperature with seasons thanks to the James Webb Space Telescope’s Mid-InfraRed Instrument (MIRI; Nixon et al. 2016). Although it would mainly provide disk-averaged measurements, MIRI, like CIRS, can measure Titan’s surface temperature by monitoring the spectral window at 19 μm .

Acknowledgments

We sincerely thank D. Jennings for helpful discussion. We are also grateful to A. Hayes for providing the bathymetry map of Ligeia Mare (published in Hayes 2016). R.E.S. is funded by the Institut Universitaire de France. T.T. is funded by Deutsche Forschungsgemeinschaft (German Research Foundation, DFG) grant TO 269/5-1.

Appendix A

Unresolved Cassini Radiometry Observations of Titan

Over the course of the Cassini mission, the RADAR operated passively as a radiometer and recorded Titan’s thermal emission at 2.2 cm from a long range (typically from a distance of 4.10^4 – 4.10^6 km) during 118 flybys. Janssen et al. (2009) already calibrated, reduced, and published 34 of these distant observations, and used them to monitor the gain stability of the radiometer amplifier. In this work, we calibrate and reduce the 84 remaining unresolved distant radiometry observations of Titan.

Figure A1 illustrates the spatial (Figure A1.a) and temporal (Figure A1.b) sampling of these measurements. The majority of them (80/118) were performed with a subspacecraft point centered on Titan’s equatorial belt (latitudes $|\delta_{\text{ssc}}| < 30^\circ$) with fewer observations on the leading side (centered at -90°E , where the radar-bright Xanadu region lies; Smith et al. 1996), than on the trailing side (Figure A1.a). Further, the boreal hemisphere was significantly more frequently observed than the austral hemisphere at high latitudes (12/118 vs 5/118, respectively, for latitudes $|\delta_{\text{ssc}}| > 50^\circ$).

Figure A1.b displays the subspacecraft latitudes of all distant radiometry observations during the course of the Cassini mission, as well as the expected surface temperature at their epoch of observation as derived from CIRS measurements (Jennings et al. 2019).

After the arrival in the cronian system during the boreal winter in 2004, the CIRS-derived surface temperature model predicts an increase in the surface temperature in the boreal hemisphere when approaching 2017, i.e., as the boreal summer solstice on Titan approached (2017 May 17). Figure A1.b also indicates the time of the day (at the subspacecraft point) when the observations were performed (dawn, day, dusk, and night). Of the 118 observations, 30 were acquired during daytime, 32 at dawn, 40 during the night, and 16 at dusk. Overall, the available data set samples Titan’s surface 2.2 cm thermal emission well both in time and space.

A.1. Data Calibration

In its passive mode, the Cassini RADAR recorded the thermal emission at 13.78 GHz (2.2 cm) from the region of the sky pointed at by its antenna in the form of time-ordered antenna temperatures. Each antenna temperature results from the convolution of the antenna radiation pattern, with the distribution of the brightness temperature of the scene observed at a given time (Figure A2.a).

During Cassini distant radiometry observations, the antenna beam radius was larger by typically 1–4 times than Titan’s disk, and the antenna beam scanned the sky along a rectangular area (typically 2° in length) centered on Titan and extending off the disk, as shown on Figure A2.a. Antenna pointing and field of view were computed with the SPICE toolkit provided by the Navigation and Ancillary Information Facility (NAIF). The antenna temperature time series resulting from the raster scan exhibits a comb shape (Figure A2.b).

The radiometry data were calibrated following Janssen et al. (2016), as discussed in the main paper (Section 2).

Contribution from the far sidelobes (from 2° to 90° away from the center of the antenna radiation pattern) was removed to keep only the signal emanating from the main beam and near-sidelobes. The zero level was determined from off-disk measurements of the raster scan (baseline of the comb in Figure A2.a), when the brightness temperature is that of the cosmic microwave background (2.7 K). The absolute calibration was achieved by considering two reference blackbody sources at known brightness temperature, namely the cold empty sky (at 2.7 K), and the warm dune fields of Titan (at a physical temperature of 93.7 K in 2005, as measured by HASI experiment on board Huygens; Fulchignoni et al. 2005) and with the emissivity of a Fresnel dielectric surface of dielectric constant about 1.6, as derived from the radiometry polarized measurements (see Janssen et al. 2016).

A.2. Data Reduction

Following the approach of Ostro et al. (2006) and Le Gall et al. (2014, 2023), the disk-integrated brightness temperature T_b^{disk} is derived from the calibrated antenna temperature T_a by comparing it to a brightness temperature distribution model including the limb-darkening $T_b^m = T_{\text{surf}} \cos^{0.04}(\theta)$ function of the angular distance to the center of the visible moon disk. More specifically, measurements are simulated accounting for their specific geometry of observation and convolving the

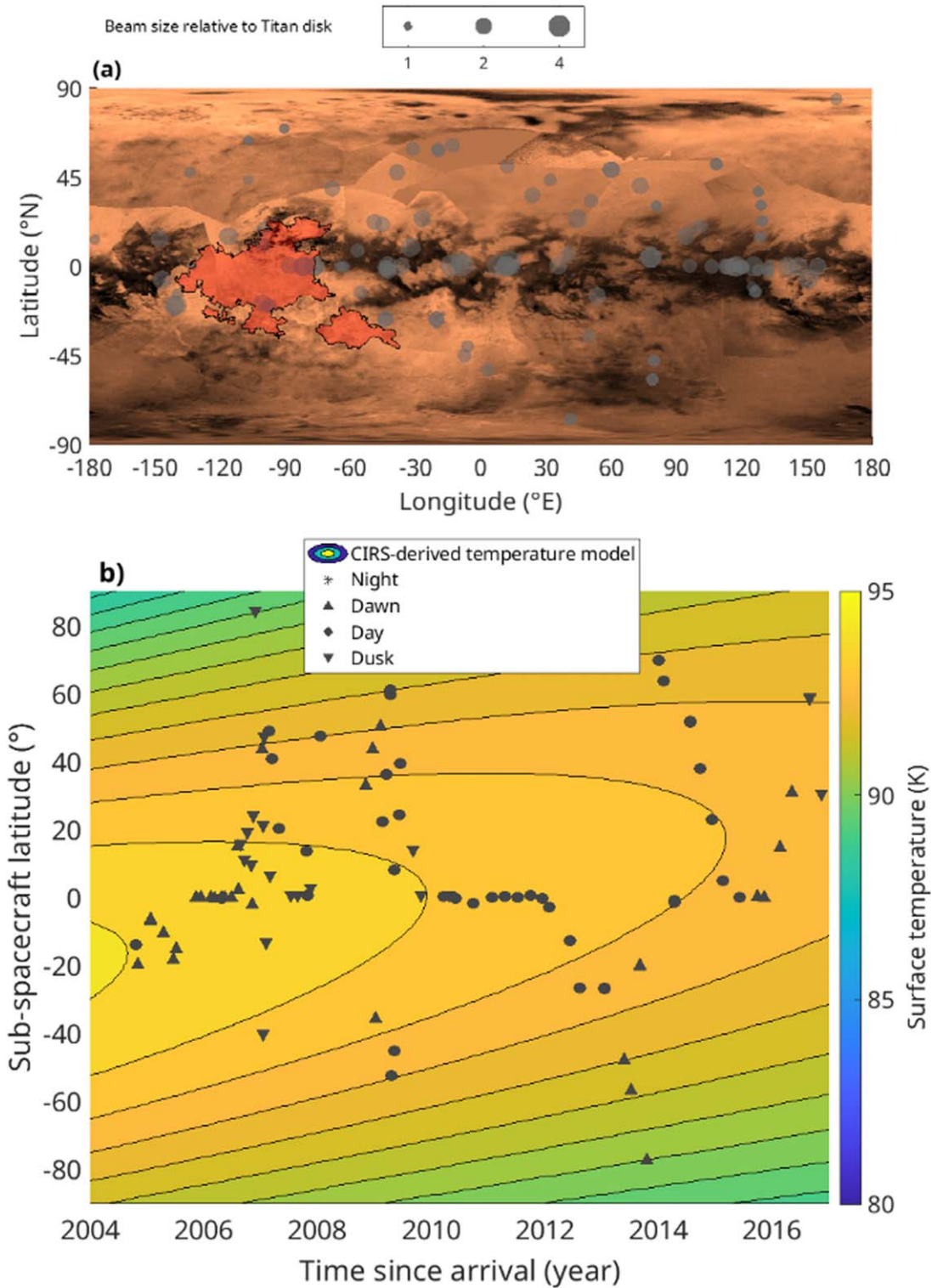


Figure A1. (a) Locations of the subspacecraft points of the 118 distant radiometry observations of Titan superimposed on a global ISS/Cassini map (gray dots). The size of the dots is related to the beam size compared to Titan’s visible disk size. Two especially low-emissivity extended regions of Titan, namely Xanadu and its annex (Janssen et al. 2016), are highlighted in red. (b) Temporal and latitudinal distribution of the distant radiometry observation subspacecraft points (gray dots). The points indicate the period of the day when the data were acquired (dawn, day, dusk, or night). The background color represents Titan’s surface temperature over the 13 years of the Cassini mission and as a function of latitude, as estimated from the CIRS-derived surface temperature model (Jennings et al. 2019).

brightness temperature model with the antenna radiation pattern. The parameters of the model are the surface temperature T_{surf} and the timing and pointing offsets. Indeed, the data reveal two systematic errors: a timing error, and a residual pointing offset that slightly varies from one epoch to

the next (Le Gall et al. 2023). The three mode parameters are then adjusted to the data to minimize the chi-squared sum of the residuals using a Levenberg–Macquardt algorithm. The disk-integrated brightness temperature is then computed as $T_b^{\text{disk}} = \frac{1}{\Omega_{\text{disk}}} \int T_b^m d\Omega$, where Ω_{disk} is the area of the visible

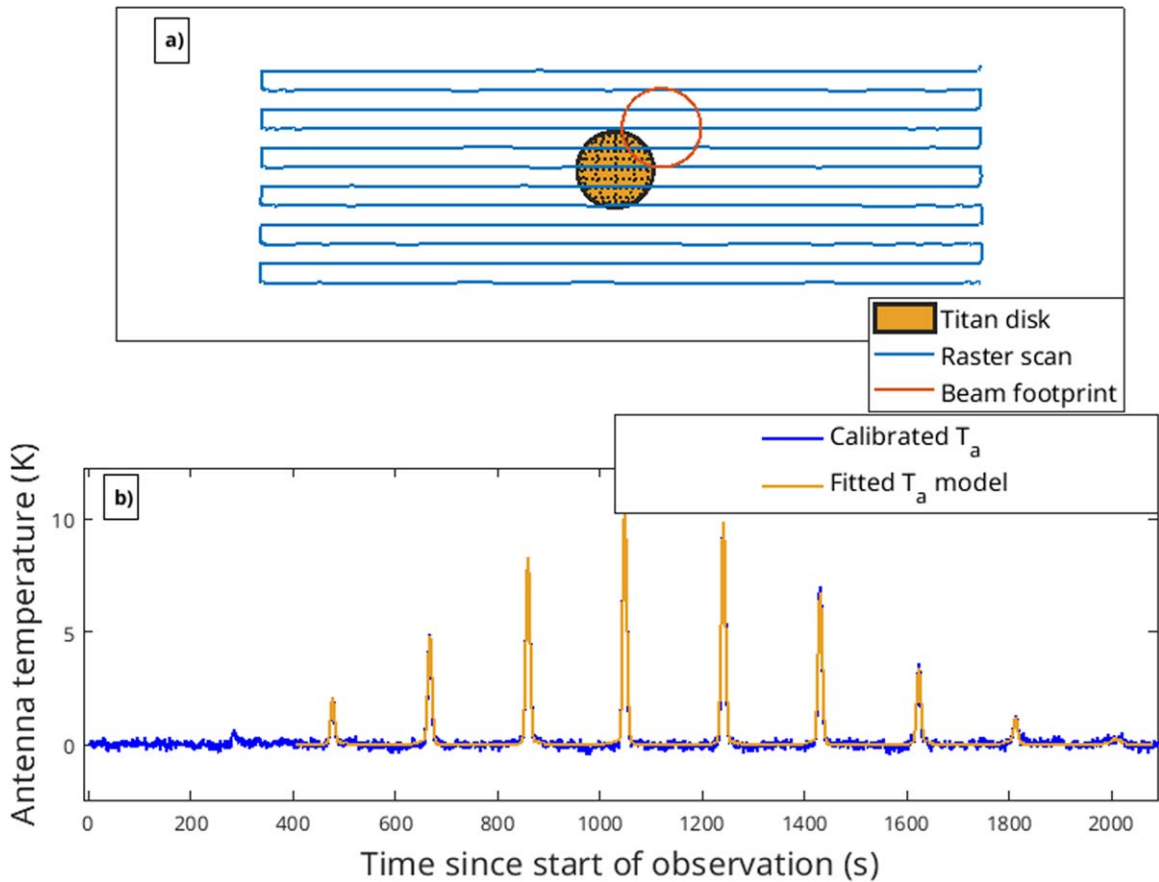


Figure A2. (a) Typical geometry of observation for distant radiometry measurements. (b) Measured antenna temperature time series and associated best-fit model.

disk of the moon, and T_b^m is the brightness temperature model fitted to the raster spectrum (see Figure A2.b). The resulting T_b^{disk} is reported in the Table A1.

After the T_b^{disk} is extracted from the data, it can be compared with the effective disk-integrated temperature of the surface in order to estimate the disk-integrated emissivity of Titan with $e^{\text{disk}} = \frac{T_b^{\text{disk}}}{T_{\text{eff}}^{\text{disk}}}$. A similar approach was followed for the analysis of distant observations of Saturn’s atmosphere-less icy satellites (Le Gall et al. 2014, 2023; Janssen et al. 2016; Bonnefoy et al. 2020). However, in the case of Titan, there is no need for a thermal model to estimate the $T_{\text{eff}}^{\text{disk}}$. Instead, we use the CIRS-derived temperature model (see Janssen et al. 2016; Equation (2) from the main text) as a proxy for $T_{\text{eff}}^{\text{disk}}$, considering that the temperature profile in the sensed near-subsurface is constant. This assumption is valid on solid surfaces, which represent most of Titan’s surface (on liquid surfaces, variations in the temperature profile are expected but are limited; see Section 4.2 and Figure 4 in the main text).

A.3. Emissivity Longitudinal Trend

Figure A3.a displays the light curve of Titan’s 2.2 cm emissivity as obtained from distant observations. It clearly shows a decrease in emissivity on the leading side of Titan that is spatially correlated to the Xanadu region. This region is indeed known for its high radar brightness and related low emissivity (Janssen et al. 2011). This latter is as low as 0.75 in the resolved radiometry mosaic, which contrasts with the high

emissivity of the dune fields surrounding the Xanadu province (Janssen et al. 2016).

Figure A3.b shows the disk-integrated emissivity of Titan as a function of the areal fraction of Xanadu in the visible disk. When extrapolating the decrease in emissivity as a function of the Xanadu filling fraction, we find an emissivity of 0.84 for a filling factor of 100%, which is very similar to the mean emissivity of Xanadu’s core (0.86 Janssen et al. 2016). The presence in the visible disk of Xanadu is the main source of variation in the derived T_b^{disk} . For the remainder of the paper, we therefore investigate a further Cassini distant radiometry data set (searching in particular for diurnal and seasonal effects) considering only the data acquired over disks where Xanadu covers less than 1% of the surface. This represents a total of 56 observations.

As a general comment, we note that the emissivity of Titan is especially high (0.92 ± 0.01) in comparison to that of the other main satellites of Saturn (Ostro et al. 2006; Le Gall et al. 2023). This is most likely the result of the global presence at the surface of Titan of a microwave-absorbing material, namely organic compounds produced by photochemistry in the atmosphere. This material also causes the very low disk-integrated radar-albedo of Titan, lying around 0.2 compared to 4.51 for Enceladus, 0.81 for Iapetus, and 0.46 for Phoebe (Le Gall et al. 2019). These organics are also very absorbent in the near-infrared ranges because the albedo of the dune fields (believed to be composed of these materials) lies below 0.1 in the near-infrared windows (Bonnefoy et al. 2016). This high surface emissivity also indicates that these layers covering the

Table A1
Characteristics of Observations for the 118 Flybys

Distant Observation ID	DATE Start Time End Time (Y M D hh:mm:ss)	Sub-Cassini Point (°E,°N)	Sub-solar Point (°E,°N)	Beam Size (Relatively to Titan Disk)	T_b^{disk} (K)	Disk-integrated Emissivity
Ta-1	2004 OCT 25 03:15:21.6 03:54:43.0	(-139.5, -14.2)	(-125.9, -23.5)	0.94	85.47 ± 1.71	0.92
Ta-2(1)	2004 NOV 6 19:49:45.9 20:51:21.8	(-140.0, -19.8)	(-52.1, -23.4)	2.96	85.25 ± 1.70	0.91
Ta-2(2)	2004 NOV 6 20:51:21.8 21:39:09.5	(-141.2, -19.8)	(-52.9, -23.4)	2.96	86.75 ± 1.73	0.93
Tc-1	2005 JAN 26 16:16:55.3 17:14:30.3	(-146.6, -7.1)	(-74.3, -22.6)	2.65	87.26 ± 1.74	0.93
Tc-2	2005 JAN 28 16:17:55.2 16:39:35.2	(150.7, -6.6)	(-119.1, -22.6)	2.85	85.52 ± 1.72	0.92
T06-1	2005 APR 18 02:31:33.0 03:24:53.0	(124.6, -10.5)	(-109.5, -21.9)	0.81	86.27 ± 1.72	0.92
T10-1	2005 JUN 19 03:52:48.7 04:25:28.7	(-100.3, -18.4)	(-68.0, -21.2)	2.25	85.11 ± 1.71	0.91
T11-1	2005 JUL 12 03:02:36.1 03:25:46.0	(53.5, -15.1)	(134.4, -21.0)	2.42	85.81 ± 1.71	0.92
T17-2	2005 NOV 12 00:15:02.2 00:31:12.2	(141.3, -0.1)	(-115.2, -19.6)	2.75	86.87 ± 1.73	0.93
T17-3	2005 NOV 12 20:49:59.8 21:26:39.7	(117.9, -0.1)	(-134.7, -19.6)	3.12	87.56 ± 1.75	0.93
T19-1	2005 DEC 13 20:18:54.7 20:39:24.6	(155.2, -0.3)	(-112.8, -19.2)	2.42	87.17 ± 1.74	0.94
T19-2	2005 DEC 15 04:01:44.9 04:53:14.9	(116.5, -0.2)	(-142.9, -19.2)	2.80	88.18 ± 1.76	0.95
T21-1	2006 FEB 15 13:54:45.5 14:17:15.5	(146.1, -0.2)	(-109.4, -18.5)	2.81	87.7 ± 1.75	0.94
T21-2	2006 FEB 16 06:57:05.1 07:15:45.1	(125.6, -0.2)	(-125.4, -18.5)	2.94	85.60 ± 1.71	0.92
T12-1(1)	2006 MAR 14 11:51:26.7 12:18:56.7	(-76.3, -0.3)	(3.8, -18.1)	2.91	86.19 ± 1.72	0.93
T22-1(2)	2006 MAR 14 12:24:16.7 12:51:26.7	(-76.6, -0.3)	(3.3, -18.1)	2.90	86.68 ± 1.73	0.93
T23-1(1)	2006 APR 26 17:47:43.9 18:27:43.9	(12.0, -0.2)	(108.8, -17.6)	3.17	85.10 ± 1.70	0.91
T23-1(2)	2006 APR 26 18:29:03.9 19:08:03.9	(11.9, -0.2)	(108.2, -17.6)	3.15	84.30 ± 1.68	0.90
T23-2	2006 APR 29 17:35:41.3 18:09:19.2	(12.8, -0.3)	(41.5, -17.5)	0.71	86.08 ± 1.72	0.92
T24-1(1)	2006 MAY 16 09:44:53.1 10:13:13.1	(-81.6, -0.2)	(25.7, -17.3)	2.65	84.51 ± 1.69	0.91
T24-1(2)	2006 MAY 16 10:13:43.1 10:45:33.0	(-81.9, -0.2)	(25.2, -17.3)	2.64	86.74 ± 1.73	0.93
T25-1	2006 JUN 30 02:30:54.4 03:35:44.4	(14.4, -0.3)	(97.8, -16.7)	1.98	86.70 ± 1.73	0.93
T26-1	2006 AUG 3 03:21:08.6 04:00:18.6	(-116.1, 14.9)	(50.8, -16.3)	2.54	83.80 ± 1.67	0.90
T27-1	2006 AUG 13 11:06:48.0 11:46:17.9	(13.2, 2.3)	(178.1, -16.2)	3.60	88.28 ± 1.76	0.95
T27-2	2006 AUG 22 18:08:04.8 19:11:54.8	(94.8, 15.4)	(-31.5, -16.0)	2.43	86.33 ± 1.72	0.93
T29-1	2006 SEP 21 07:59:14.5 08:42:52.5	(-99.9, 10.9)	(21.9, -15.6)	1.48	85.01 ± 1.70	0.91
T30-1	2006 OCT 7 08:16:14.7 08:50:13.7	(-99.7, 18.8)	(21.0, -15.4)	1.42	84.33 ± 1.68	0.91
T32-1	2006 NOV 4 21:48:54.9 22:26:28.9	(-32.5, 9.5)	(-32.5, 9.5)	2.88	85.63 ± 1.71	0.92
T32-2	2006 NOV 6 20:45:34.9 21:42:33.8	(-42.4, -2.3)	(52.8, -15.0)	1.94	86.19 ± 1.73	0.92
T33-1	2006 NOV 13 21:26:10.0 21:59:34.0	(44.4, 23.8)	(-105.3, -14.9)	2.68	86.64 ± 1.73	0.93
T37-1	2006 NOV 25 05:17:24.7 06:40:43.7	(163.5, 84.2)	(-1.1, -14.7)	1.14	86.30 ± 1.72	0.93
T37-2	2007 JAN 12 02:21:26.9 03:00:25.5	(-107.1, 43.7)	(-0.1, -14.1)	0.72	83.98 ± 1.67	0.91
T37-3	2007 JAN 15 17:02:17.5 17:27:44.5	(-5.8, -40.5)	(-81.3, -14.0)	1.24	84.97 ± 1.69	0.91
T37-4	2007 JAN 18 20:37:40.8 21:29:03.8	(-45.0, 20.9)	(-152.6, -14.0)	1.72	83.99 ± 1.67	0.90
T37-5	2007 JAN 21 02:02:56.6 02:54:59.6	(-38.7, 47.2)	(157.2, -14.0)	2.02	86.50 ± 1.73	0.93
T38-1	2007 FEB 3 09:31:51.3 09:46:51.3	(-55.3, -13.4)	(-142.5, -13.8)	1.37	84.83 ± 1.69	0.91
T39-1(1)	2007 FEB 26 14:37:53.6 15:35:53.6	(60.1, 48.7)	(53.8, -13.4)	2.09	86.91 ± 1.73	0.94
T39-1(2)	2007 FEB 26 15:35:54.6 16:30:04.6	(59.7, 48.7)	(52.9, -13.4)	2.10	86.79 ± 1.73	0.94
T40-1	2007 MAR 5 13:54:47.8 14:15:54.8	(40.5, 6.1)	(-103.0, -13.3)	1.73	85.36 ± 1.71	0.92
T40-3	2007 MAR 13 22:51:21.2 23:06:21.2	(73.5, 40.7)	(68.3, -13.2)	2.08	85.06 ± 1.70	0.92
T43-1	2007 APR 29 12:06:33.8 12:21:14.8	(100.8, 20.0)	(98.8, -12.5)	1.64	86.86 ± 1.73	0.93
T48-1	2007 JUL 15 14:49:00.6 15:21:37.6	(-88.2, 0.3)	(160.3, -11.4)	2.35	83.79 ± 1.67	0.90
T49-1	2007 AUG 27 03:07:29.3 03:30:31.3	(7.8, 0.3)	(-77.9, -10.8)	3.29	81.74 ± 1.63	0.88
T51-1	2007 OCT 21 01:01:43.4 01:41:08.4	(-177.4, 13.4)	(123.9, -10.0)	0.73	86.01 ± 1.72	0.92
T51-2	2007 OCT 27 10:12:28.5 10:58:13.5	(-8.5, 0.5)	(-20.0, -9.9)	3.61	84.53 ± 1.69	0.91
T52-1	2007 NOV 16 03:20:15.5 04:07:25.5	(-9.7, 2.4)	(-104.4, -9.6)	2.56	86.07 ± 1.72	0.92
T57-1	2008 JAN 22 03:25:37.6 03:42:17.6	(-133.9, 47.4)	(-174.8, -8.6)	1.11	84.97 ± 1.69	0.92

Table A1
(Continued)

Distant Observation ID	DATE Start Time End Time (Y M D hh:mm:ss)	Sub-Cassini Point (°E, °N)	Sub-solar Point (°E, °N)	Beam Size (Relatively to Titan Disk)	T_b^{disk} (K)	Disk-integrated Emissivity
T92-1	2008 NOV 6 16:06:44.2 16:55:24.2	(51.0, 32.8)	(137.4, -4.1)	1.46	86.27 ± 1.72	0.93
T98-1	2008 DEC 23 22:57:03.2 23:30:23.2	(31.9, 43.4)	(151.5, -3.4)	1.25	86.05 ± 1.72	0.93
T99-1	2009 JAN 7 18:15:00.1 19:06:20.1	(49.9, -35.6)	(177.6, -3.2)	1.30	87.23 ± 1.74	0.93
T103-1	2009 FEB 11 01:35:15.1 02:01:35.2	(12.0, 50.3)	(124.3, -2.6)	1.48	85.88 ± 1.71	0.93
T104-1	2009 FEB 20 18:20:15.1 18:45:45.1	(-48.9, 22.3)	(-94.3, -2.5)	1.79	84.82 ± 1.69	0.91
T106-1	2009 MAR 19 13:50:06.6 14:17:46.6	(23.6, 36.1)	(21.1, -2.1)	1.79	86.07 ± 1.72	0.92
T108-1	2009 APR 15 21:57:31.8 22:16:21.8	(-13.1, 60.9)	(124.8, -1.6)	1.58	85.41 ± 1.70	0.92
T108-2	2009 APR 16 21:09:26.2 21:25:56.2	(-31.0, 59.4)	(103.0, -1.6)	1.45	84.50 ± 1.69	0.91
T109-1	2009 APR 22 21:29:58.5 21:48:18.5	(3.4, -52.4)	(-32.5, -1.5)	1.35	85.54 ± 1.71	0.92
T110-1	2009 MAY 8 20:22:37.7 20:46:22.7	(-7.6, -45.3)	(-32.3, -1.3)	1.38	85.50 ± 1.71	0.92
T110-2	2009 MAY 11 19:22:12.9 20:16:22.9	(-56.6, 7.8)	(-99.2, -1.2)	1.32	84.12 ± 1.68	0.90
T112-1	2009 JUN 11 18:02:52.9 18:54:32.9	(-26.8, 24.1)	(-76.8, -0.8)	2.26	84.84 ± 1.69	0.91
T113-1	2009 JUN 18 23:02:45.5 23:24:50.5	(-68.3, 39.1)	(120.8, -0.7)	2.02	85.19 ± 1.70	0.92
T117-1	2009 SEP 7 17:58:03.9 18:38:03.8	(-147.5, 13.7)	(99.1, 0.6)	2.21	86.665 ± 1.73	0.93
T120-1	2009 OCT 29 15:48:43.2 16:29:33.2	(96.1, 0.3)	(8.8, 1.4)	1.48	85.85 ± 1.71	0.92
T128-1	2010 MAR 22 06:14:54.0 07:10:44.1	(35.8, 0.2)	(10.9, 3.6)	2.19	87.19 ± 1.74	0.94
T130-1	2010 APR 30 03:51:15.9 04:42:20.9	(-42.9, 0.3)	(-146.1, 4.1)	2.43	86.44 ± 1.72	0.92
T132-1	2010 JUN 7 14:22:46.2 15:06:06.2	(106.4, -0.4)	(67.2, 4.7)	1.53	87.31 ± 1.74	0.94
T138-1	2010 SEP 26 09:20:59.5 11:10:59.5	(127.6, -1.9)	(88.7, 6.3)	1.01	86.87 ± 1.73	0.93
T144-1	2011 JAN 29 03:16:50.6 04:40:10.6	(-36.8, -0.0)	(156.3, 8.1)	2.33	85.62 ± 1.71	0.92
T147-1	2011 APR 20 16:06:14.1 17:16:44.1	(132.5, 0.2)	(118.0, 9.3)	0.89	86.07 ± 1.72	0.93
T150-1(1)	2011 JUL 8 22:08:29.8 22:49:19.8	(-64.7, -0.1)	(131.4, 10.4)	0.82	84.57 ± 1.69	0.90
T150-1(2)	2011 JUL 8 22:51:59.8 23:32:59.8	(-63.6, -0.1)	(130.7, 10.4)	0.81	84.51 ± 1.69	0.91
T150-1(3)	2011 JUL 8 23:36:29.8 00:16:39.8	(-62.5, -0.1)	(130.0, 10.4)	0.81	84.25 ± 1.68	0.90
T154-1	2011 OCT 4 17:57:12.8 18:58:22.8	(-13.6, 0.3)	(-48.9, 11.6)	3.46	88.22 ± 1.76	0.94
T158-1(1)	2011 DEC 15 21:40:46.3 22:13:06.3	(120.7, -0.5)	(124.4, 12.5)	1.28	86.11 ± 1.72	0.93
T158-1(2)	2011 DEC 15 22:15:46.3 22:49:16.3	(120.3, -0.5)	(123.9, 12.5)	1.30	86.52 ± 1.73	0.93
T160-1(1)	2012 FEB 1 01:23:32.5 02:36:52.5	(132.5, -3.0)	(140.9, 13.1)	0.91	86.40 ± 1.72	0.93
T160-1(2)	2012 FEB 1 02:35:12.5 03:35:12.5	(131.6, -2.9)	(139.9, 13.1)	0.93	86.76 ± 1.73	0.93
T167-1(1)	2012 JUN 8 17:28:54.1 18:02:54.0	(126.6, -12.9)	(120.2, 14.8)	1.05	86.47 ± 1.72	0.93
T167-1(2)	2012 JUN 8 18:08:24.0 18:39:24.0	(126.2, -12.9)	(119.6, 14.8)	1.06	86.34 ± 1.72	0.93
T170-1(1)	2012 AUG 10 21:02:05.4 21:45:55.4	(-43.8, -26.8)	(136.3, 15.5)	1.86	85.67 ± 1.71	0.92
T170-1(2)	2012 AUG 10 22:01:35.4 22:36:35.4	(-43.5, -26.7)	(135.5, 15.5)	1.85	86.11 ± 1.72	0.93
T179-1(1)	2013 JAN 17 05:29:01.0 06:02:50.9	(-20.4, -27.2)	(143.7, 17.4)	1.96	85.93 ± 1.71	0.93
T179-1(2)	2013 JAN 17 06:07:20.9 06:40:40.9	(-20.3, -26.8)	(143.1, 17.4)	1.95	85.62 ± 1.71	0.92
T190-1(1)	2013 MAY 25 19:15:53.4 19:42:53.4	(79.8, -47.8)	(124.9, 18.8)	1.09	85.23 ± 1.70	0.92
T190-1(2)	2013 MAY 25 19:48:33.4 20:15:33.4	(79.4, -47.8)	(124.4, 18.8)	1.10	85.53 ± 1.71	0.92
T194-1(1)	2013 JUL 12 15:54:40.2 16:30:10.2	(79.3, -56.9)	(125.2, 19.3)	1.12	85.14 ± 1.70	0.92
T194-1(2)	2013 JUL 12 16:32:10.2 17:07:10.2	(78.8, -56.9)	(125.2, 19.3)	1.12	85.06 ± 1.70	0.92
T197-1(1)	2013 SEP 2 06:01:20.9 06:32:40.9	(-97.2, -20.4)	(42.8, 19.7)	1.63	84.22 ± 1.68	0.91
T197-1(2)	2013 SEP 2 06:41:00.9 07:15:30.8	(-97.7, -20.2)	(42.1, 19.8)	1.62	84.44 ± 1.68	0.91
T198-1(1)	2013 OCT 16 02:29:00.8 03:04:00.8	(41.4, -77.5)	(134.0, 20.2)	1.00	84.82 ± 1.69	0.92
T198-1(2)	2013 OCT 16 03:05:40.8 03:41:30.8	(41.0, -77.5)	(133.5, 20.2)	1.01	84.88 ± 1.69	0.92
T200-1(1)	2013 DEC 31 12:00:44.8 12:34:24.8	(-90.2, 69.5)	(-148.3, 20.9)	0.77	85.34 ± 1.70	0.92
T200-1(2)	2013 DEC 31 12:35:44.8 13:10:44.8	(-90.6, 69.6)	(-148.8, 20.9)	0.76	85.44 ± 1.70	0.92
T201-1(1)	2014 FEB 1 10:04:40.3 10:38:20.3	(-106.7, 63.5)	(-147.9, 21.2)	0.76	85.35 ± 1.70	0.92
T201-1(2)	2014 FEB 1 10:40:50.3 11:12:50.2	(-107.1, 63.5)	(-148.4, 21.2)	0.75	85.39 ± 1.70	0.92

Table A1
(Continued)

Distant Observation ID	DATE Start Time End Time (Y M D hh:mm:ss)	Sub-Cassini Point (°E,°N)	Sub-solar Point (°E,°N)	Beam Size (Relatively to Titan Disk)	T_b^{disk} (K)	Disk-integrated Emissivity
T203-1(1)	2014 APR 11 18:14:16.2 18:47:11.2	(−43.2, −1.5)	(88.8, 21.8)	2.03	85.34 ± 1.70	0.92
T203-1(2)	2014 APR 11 19:04:16.2 19:34:16.2	(−43.5, −1.5)	(88.0, 21.8)	2.03	84.89 ± 1.69	0.92
T206-1(1)	2014 JUL 22 15:53:37.2 16:27:47.2	(108.7, 51.5)	(−48.5, 22.6)	1.23	86.58 ± 1.73	0.93
T206-1(2)	2014 JUL 22 16:29:27.2 17:04:27.2	(108.3, 51.5)	(−49.1, 22.6)	1.25	86.80 ± 1.73	0.93
T208-1(1)	2014 SEP 23 16:55:35.5 17:31:25.5	(127.9, 37.7)	(−29.8, 23.1)	0.86	86.2 ± 1.72	0.93
T208-1(2)	2014 SEP 23 17:32:55.5 18:09:45.5	(127.5, 37.6)	(−30.4, 23.1)	0.88	86.31 ± 1.72	0.93
T210-1(1)	2014 DEC 12 11:48:55.7 12:32:45.7	(129.8, 22.8)	(−28.6, 23.6)	0.93	86.59 ± 1.73	0.93
T210-1(2)	2014 DEC 12 12:38:05.7 13:15:45.6	(129.2, 22.7)	(−29.3, 23.6)	0.95	86.18 ± 1.72	0.93
T212-1(1)	2015 FEB 17 11:28:12.8 11:59:12.8	(78.3, 4.7)	(−98.6, 24.1)	3.25	86.50 ± 1.73	0.93
T212-1(2)	2015 FEB 17 12:11:12.8 12:52:32.8	(77.8, 4.7)	(−99.4, 24.1)	3.27	89.68 ± 1.79	0.97
T217-1(1)	2015 JUN 9 03:20:06.3 03:48:06.3	(114.1, −0.3)	(−95.9, 24.8)	2.06	86.27 ± 1.72	0.93
T217-1(2)	2015 JUN 9 04:09:16.3 04:37:36.3	(113.2, −0.3)	(−96.7, 24.8)	2.08	86.16 ± 1.72	0.93
T222-1(1)	2015 SEP 27 18:37:24.5 19:07:44.5	(−132.4, 0.1)	(−70.1, 25.3)	0.65	84.04 ± 1.68	0.91
T222-1(2)	2015 SEP 27 19:19:14.5 19:49:54.5	(−132.9, 0.1)	(−70.8, 25.3)	0.64	83.98 ± 1.67	0.91
T225-1(1)	2015 NOV 14 16:36:41.1 17:28:41.1	(118.2, −0.2)	(−70.5, 25.5)	0.85	86.12 ± 1.72	0.93
T225-1(2)	2015 NOV 14 17:38:21.1 18:23:41.1	(117.5, −0.1)	(−71.4, 25.5)	0.88	86.27 ± 1.72	0.93
T232-1(1)	2016 FEB 18 10:17:09.9 10:53:49.9	(128.9, 14.6)	(−68.6, 25.9)	0.87	86.27 ± 1.72	0.93
T232-1(2)	2016 FEB 18 10:55:29.9 11:31:19.8	(128.4, 14.6)	(−69.2, 25.9)	0.88	86.57 ± 1.73	0.93
T235-1(1)	2016 MAY 8 05:27:02.0 06:02:52.0	(129.2, 30.9)	(−67.5, 26.2)	0.90	86.56 ± 1.73	0.93
T235-1(2)	2016 MAY 8 06:08:02.0 06:40:22.0	(128.7,30.8)	(−68.1, 26.2)	0.92	86.60 ± 1.73	0.93
T241-1(1)	2016 AUG 28 23:07:30.8 23:39:10.8	(−19.6,58.7)	(−88.9, 26.5)	1.34	86.68 ± 1.73	0.94
T241-1(2)	2016 AUG 28 23:46:40.8 00:14:40.8	(−19.5,58.4)	(−89.5, 26.5)	1.33	86.03 ± 1.72	0.93
T249-1(1)	2016 NOV 15 16:56:41.2 17:30:01.2	(81.3,30.2)	(−64.1, 26.6)	0.92	86.55 ± 1.73	0.93
T249-1(2)	2016 NOV 15 17:37:46.2 18:10:01.1	(80.7,30.2)	(−64.7, 26.6)	0.94	86.27 ± 1.72	0.93

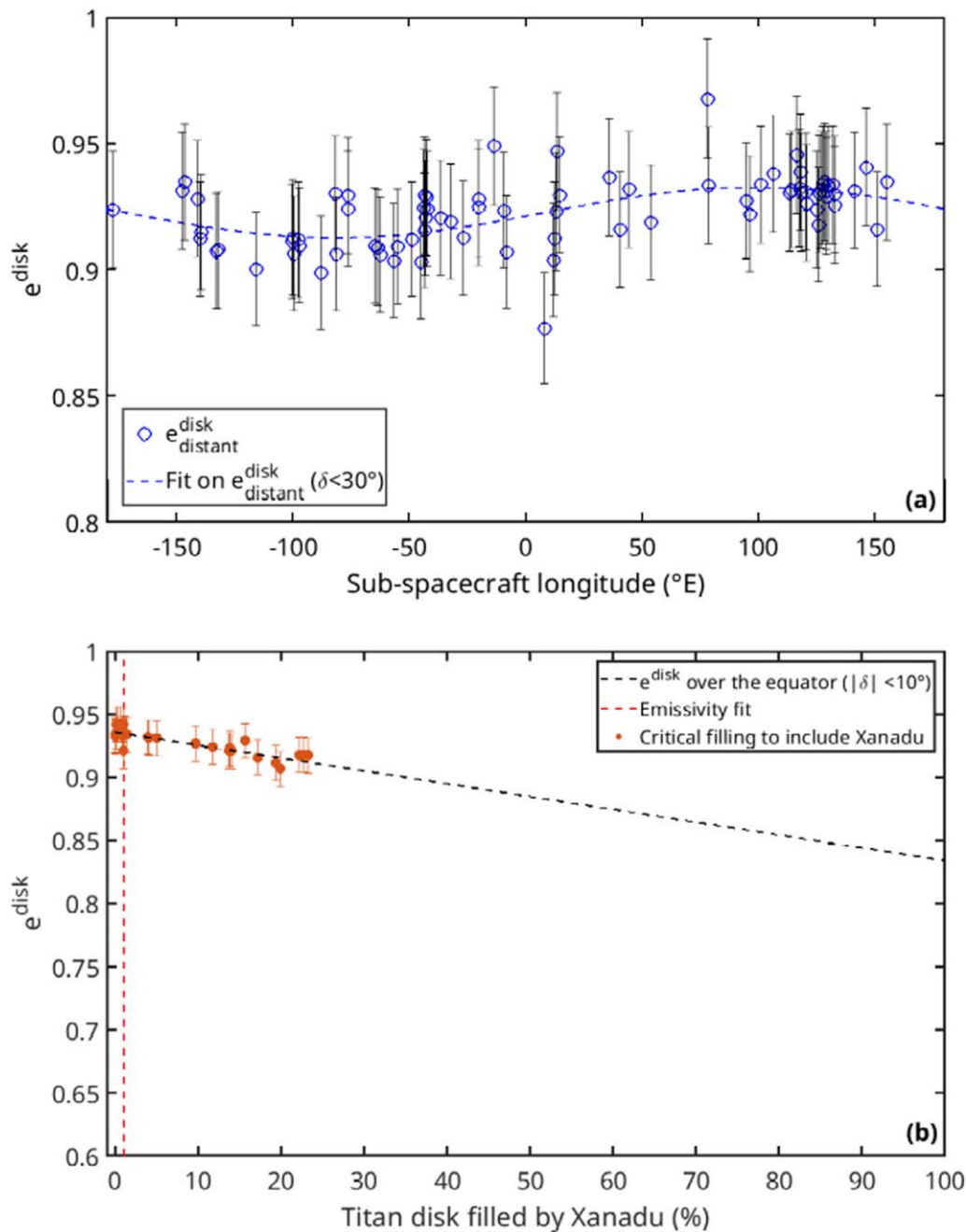


Figure A3. (a) 2–2 cm disk-integrated emissivity of Titan as a function of longitude. The solid line shows the adjustment of a sinusoidal function to the data; it indicates a minimum emissivity of 0.93 centered at -89°E in the core of the Xanadu region. (b) Disk-integrated emissivity as a function of the fraction of Xanadu in the visible disk.

dark regions are up to several decimeters thick because the radiometer does not see the surface below this material.

A.4. No Diurnal Variations

Distant Cassini radiometry observations also offer the opportunity of investigating diurnal variations in the surface temperature. Such an investigation is not possible with spatially resolved observations due to the way in which they were calibrated and assembled into a mosaic (see Section 2 of the main paper). Relying on CIRS observations, Cottini et al. (2012) have found that the surface temperature of the tropical regions of Titan undergoes a daily fluctuation of 1.0–1.5 K,

reaching a maximum in the late afternoon. This fluctuation shows a minimum of surface temperature in the morning (around 4 am) and a broad flattish maximum in the afternoon until 8 pm. Cottini et al. (2012) indicate that this could be explained by a retro-warming of the surface by the deeper layers that were heated earlier in the day by conduction from the surface. Cottini et al. (2012) compare their results with an atmospheric circulation model (Tokano 2005) and found that their observed diurnal signal corresponds to a ground thermal inertia of 300–600 MKS, pointing to a porous icy surface.

Figure A4 shows the 2–2 cm disk-integrated temperature as a function of the local hour of the subspacecraft point. Only data acquired over disks devoid of Xanadu and with a

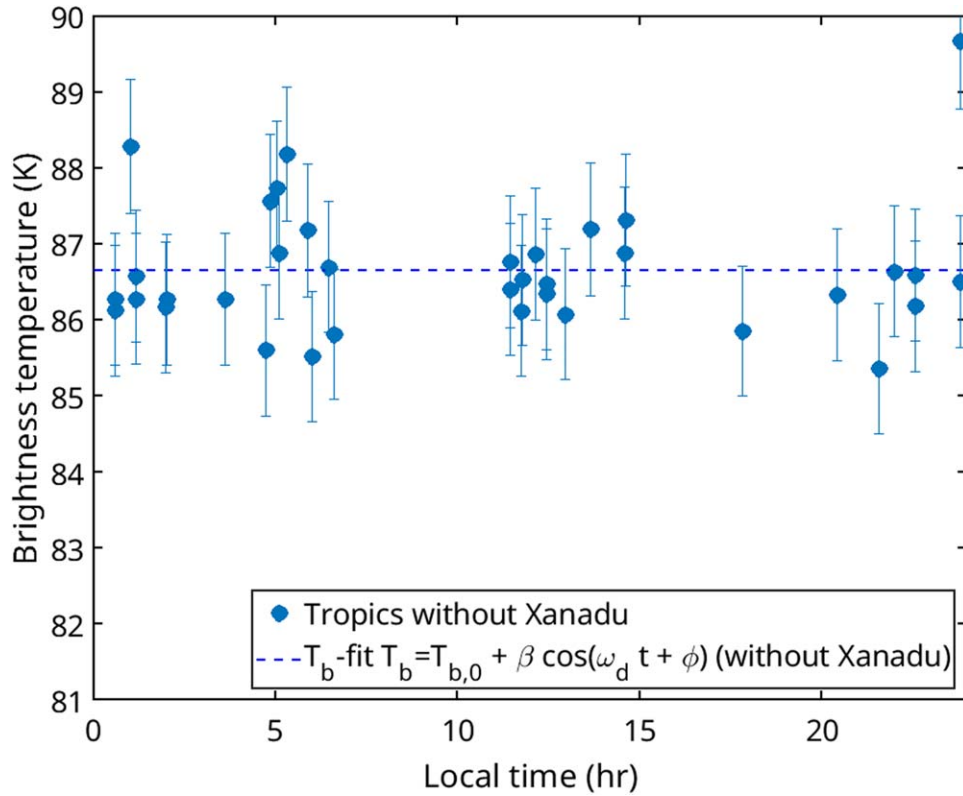


Figure A4. Evolution of the brightness temperature against the local time of the subspacecraft point outside of Xanadu’s influence. The dashed line is the results of a sinusoidal function fitted to the data in order to determine the period, the amplitude, and the hour of the temperature maximum.

subspacecraft point in the equatorial belt (where the diurnal signal should be more pronounced) were considered here.

No evidence for the presence of a diurnal fluctuation of the temperature stands out, suggesting that the radiometer probes the surface at depths larger than the daily thermal skin depth, which is estimated to be in the range $\delta_{\text{th}}^{\text{day}} > 0.1\text{--}1$ m depending on the type of the terrain types and their properties, here, for example, dunes and hummocky terrain, respectively.

A.5. Global Variations in Temperature at High Latitudes

Twelve distant (unresolved) observations were recorded in Titan’s polar regions. Figure A5 presents the evolution of the brightness temperature along the cronian year compared to the CIRS model prediction of the disk-integrated brightness temperature (Janssen et al. 2016; see Equation (2) of the main

text). $T_{\text{CIRS}}^{\text{disk}}$ was estimated mapping the CIRS-derived model onto spacecraft view coordinates and averaging the surface temperature in the same way as for the brightness temperature over the visible disk (see Section A.2)

In the boreal hemisphere (Figure A5), both temperatures (T_b^{disk} and $T_{\text{CIRS}}^{\text{disk}}$) slowly increase between 2004 and 2017, as expected with the arrival of summer. In the austral region, in contrast, we observe a decrease in both temperatures as the hemisphere enters winter.

The possibly slower rate in the temperature change at the boreal pole may be related to surface moisture that increases the surface thermal inertia, as suggested by Jennings et al. (2019). Distant observations at the boreal pole are thus consistent with the resolved ones in the solid RoIs (see Figure 3 from the main text), which is expected as most of Titan’s boreal pole is covered by solid terrain.

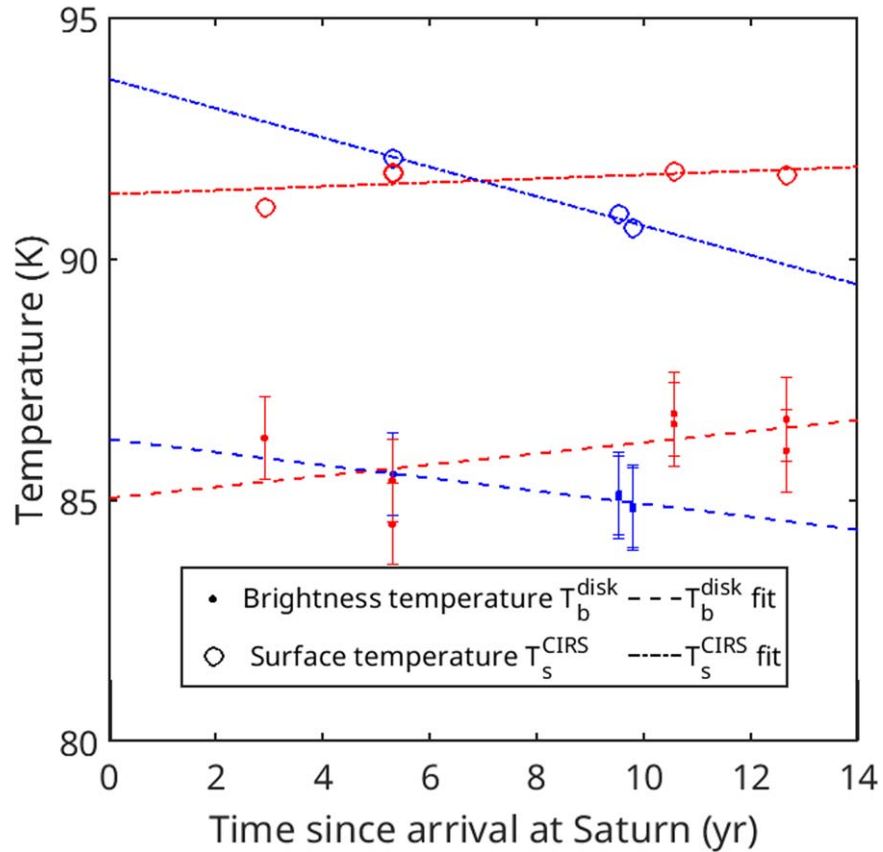


Figure A5. Seasonal variations in the disk-integrated brightness temperature in the polar regions (boreal in red, and austral in blue) and the predictions from CIRS surface temperature model integrated over the visible disk. The measurements indicate a decrease in both temperatures in the austral hemisphere and an increase in both temperatures in the boreal polar regions over the course of the Cassini mission. The boreal hemisphere is color-coded in red, and blue represents the austral hemisphere.

Appendix B

Cassini Resolved Radiometry Observations

B.1. Observations of the Boreal Polar Regions

Figure B1 presents the locations of the different swaths (see the swath characteristics reported in Table B1), specifying the beams over Ligeia Mare for each flyby overplotted on the bathymetry map (Hayes 2016). Each footprint in the swaths is colored according to the effective temperature computed from the measured brightness temperature and a two-layer emissivity model (see Section 3.2 in the main paper). We note that within a given observation, the recorded sea temperatures are relatively spatially constant, showing a dispersion smaller than 1 K, and they are mainly related to variations in the sea depth. The decrease in temperature over Ligeia Mare reported in the main text of this article is visible in Figure B1, with the notable exception of T25 and T92, which are much cooler and warmer, respectively, than the following observations.

To understand the deviations in the temperature values recorded during T25 and T92 over Ligeia Mare, we searched for possibly systematic bias during these flybys by comparing their measurements to overlapping observations over solid terrains. More specifically, we identified a region west of Kraken Mare where T25 overlaps with the swaths of T16, T18, T19, T28, T29, and T30, similar to the region south of Ligeia Mare, where T92 overlaps with T28, T30, T86, T91, T104, and

T126. Figures B2(a) and (b) display all the mean brightness temperatures recorded in these two regions.

In both regions, the temperatures of T25 and T92 are very similar to those of the other observations, especially those in close temporal proximity, suggesting that these two measurements are not biased. We thus decided to keep them in the analysis.

B.2. RADAR Cross Section on Ligeia Mare

To estimate the effective temperature of Ligeia Mare, we assume a constant emissivity with time (see Section 3 in the main paper). As a sanity check, all SAR measurements over Ligeia Mare were scrutinized. We recall that active RADAR and passive radiometry observations are generally anticorrelated (by virtue of Kirchhoff's law of thermal radiation), so that a change in the cross section (σ_0) may also indicate a change in emissivity (rather than a change in temperature).

Figure B3 exhibits the σ_0 measured over Ligeia Mare and averaged on the radiometry footprints. It confirms that there is no significant increase in the σ_0 with time that could be indicative of a decrease in emissivity (the exception of T91 is due to the viewing geometry of this pass, which was dedicated to altimetry). Transient phenomena have been observed in Ligeia Mare with high σ_0 (Hofgartner et al. 2016); however, they are both rare and very localized, and are unlikely to affect the average emissivity of the whole sea.

Table B1
Characteristics of the Cassini Radiometry Flybys over Ligeia Mare and the Solid Terrains.

Flyby	Date (yy/mm/dd)	L_s (deg) ^a	Incidence Angle θ (deg)	Range of Footprint Dimensions $b \times a$		Polarization Angle ϕ	
				(km \times km)		(deg) ^b	
				Ligeia Mare	Solid Terrains	Ligeia Mare	Solid Terrains
T25	07/02/22	331	15–21	(26–34) \times (26–136)	...	196–237	...
T28	07/04/10	333	13–20	(15–19) \times (15–79)	(18–24) \times (18–108)	167–180	167–214
T29	07/04/26	334	16–25	(12–15) \times (12–75)	...	170–179	...
T30	07/05/12	335	16–24	...	(15–17) \times (15–75)	...	17–41
T64 ^c	09/12/28	4	31–38	(7–9) \times (7–46)	...	180	...
T86	12/09/26	37	35–42	(9–10) \times (9–52)	(8–9) \times (7–47)	24–42	15–20
T91	13/05/23	42	0–3	(10–12) \times (10–12)	(7–9) \times (7–9)
T92	13/07/10	43.5	5–16	(12–17) \times (12–77)	(10–12) \times (9–60)	0–17	359–0
T104	14/08/21	59	5–13	(23–27) \times (23–113)	(33–34) \times (143–150)	357–3	259–276
T108	15/01/11	63	2–12	(9–11) \times (9–48)	...	194–242	...
T126	17/04/23	89	16–25	(11–13) \times (11–64)	(13–20) \times (14–93)	0–7	359–1

Notes.

^a L_s is the solar longitude. $L_s = 0^\circ$ corresponds to the vernal equinox.

^b ϕ is defined as the angle of orientation of the electric field vector about the look vector during the passive-mode measurement. The angle is 0° when the electric field vector is perpendicular to the plane of incidence as defined by the look vector and the target surface normal, and it increases counterclockwise.

^c On 2009 December 29, a Cassini downlink to the antenna complex in Madrid, Spain, was significantly affected by heavy rain. Seventy-six minutes of telemetry were lost due to both rain and an incorrect set of parameters used for the receiver (downlink controller table). Even though a second redundant playback of the spacecraft solid-state recorder was planned and executed, the redundant playback was in the same pass and was also affected. As a result, data from Titan Pass T64 were very noisy (see Figures A4–B1 in the Appendix).

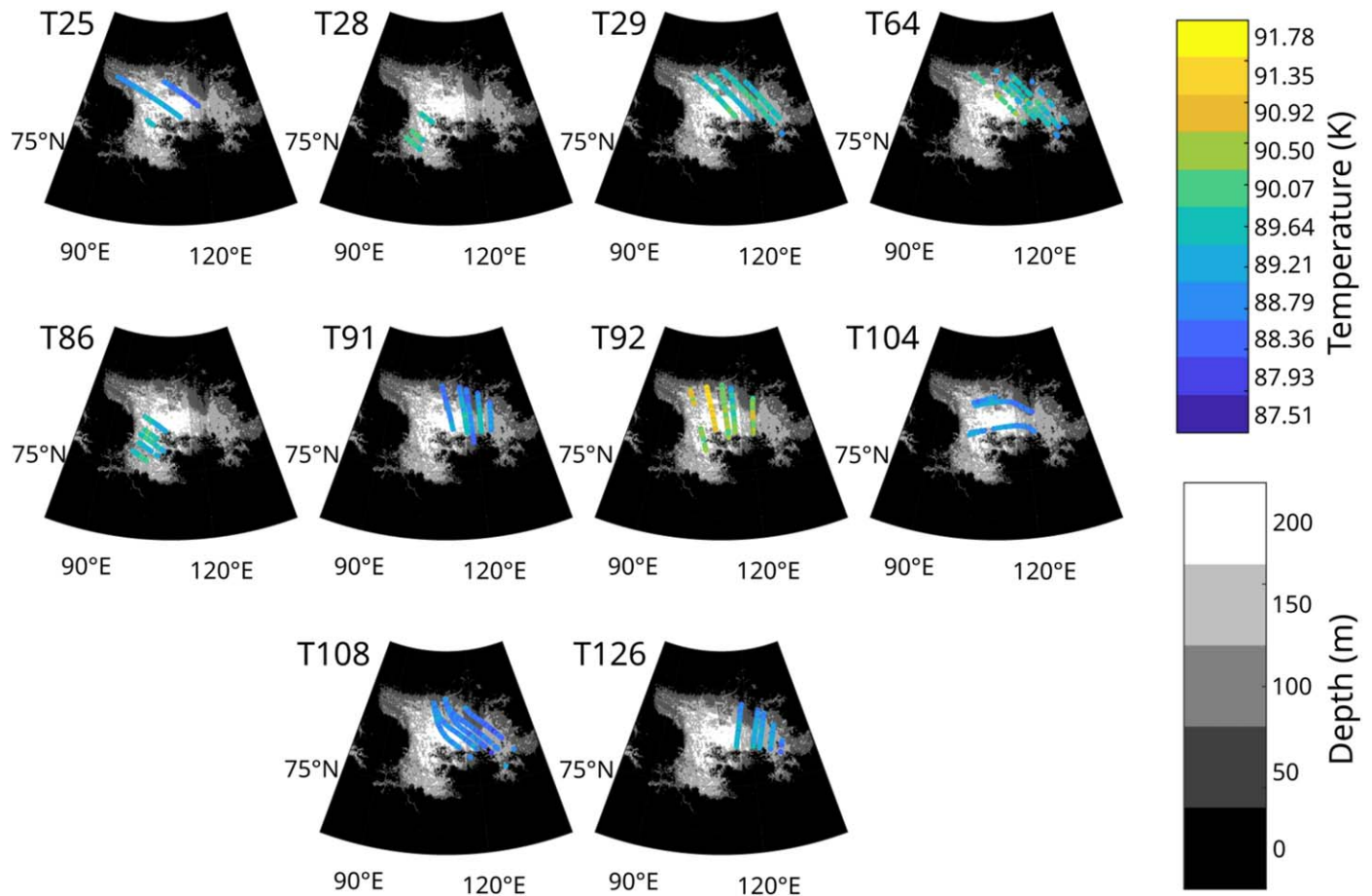


Figure B1. Detailed visualization of the Cassini flyby swaths over Ligeia Mare. Each footprint—plotted over the bathymetry map—is colored according to the recorded brightness temperature.

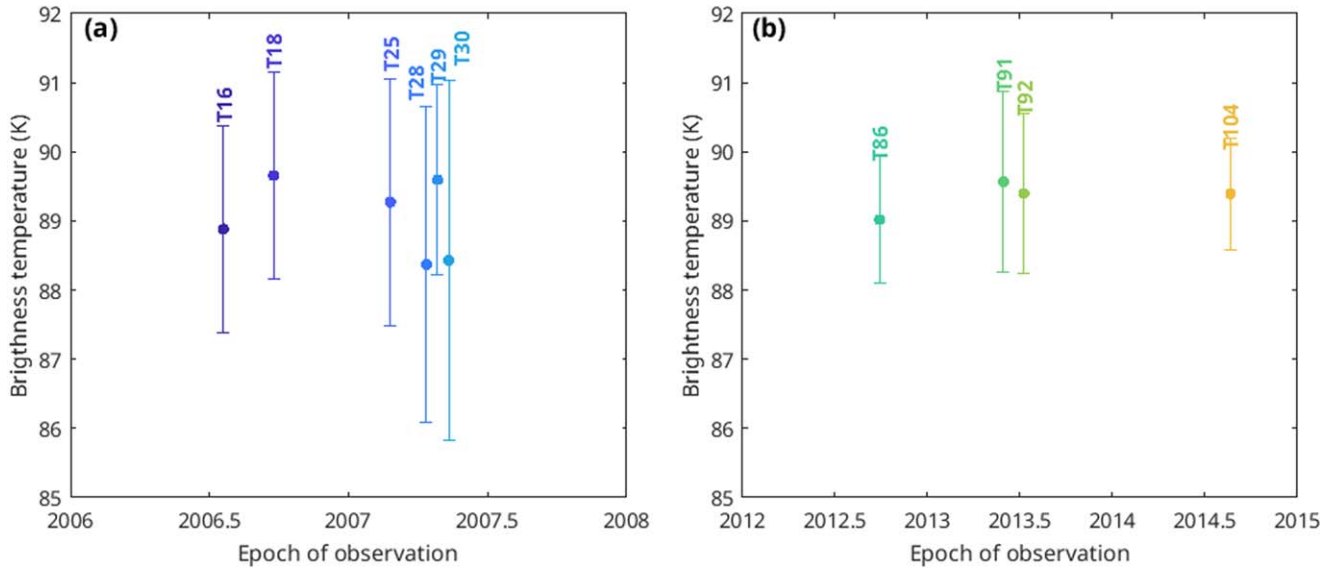


Figure B2. Variations with time in the brightness temperatures recorded over the solid terrains around (a) T25 west of Kraken Mare, and (b) T91 south of Ligeia Mare.

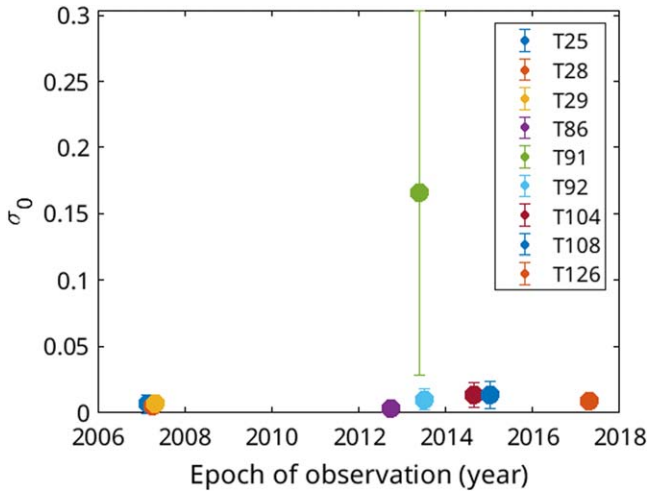


Figure B3. RADAR cross section over Ligeia Mare. The main source of variability in σ_0 resides in the viewing geometry, which is very noticeable for T91—measured in altimetry mode (at nadir). Overall, σ_0 remains relatively constant over the course of the mission.

B.3. Permittivity Variations in Ligeia Mare

We used the Fresnel coefficient as a proxy for the RADAR reflectivity at the sea surface to estimate the variation in the sea permittivity required to decrease the sea emissivity by 2%, as described in the main text (see Figure 2). We found, as illustrated in the Figure B4, that the permittivity has to decrease by about 25% for a permittivity of about 1.7 as estimated in this work from the sea composition constrained by Mastrogiuseppe et al. (2016), and by 11% for a permittivity of 4, chosen as an extreme value to provide a lower bound for the permittivity decrease.

To check that the emissivity variation derived from the radiometry observation in this work is independent of a composition change during spring (e.g., as the result of methane evaporation), we computed the emissivity and the effective temperature taking concentrations of methane between 50% and 100% into account (Figure B5). We imposed that the ethane and nitrogen concentration were dependent on

the methane concentration, while their relative concentration remained constant.

As illustrated in Figure B5, the permittivity of the sea only increases by 0.1% when the methane concentration varies between 50 and 100%. The consequence on emissivity is a decrease slightly larger than 0.1% and an increase by 0.1 K of the effective temperature, much smaller than the 2% derived from the observation and the CIRS surface temperature in the main text (see Figure 2). This shows that the variation in methane concentration cannot cause the observed variation in emissivity over the boreal spring.

These two results hence support that the decrease in the brightness temperature measured over Ligeia Mare is unlikely to be related to a variation in the sea permittivity and the global composition, and that this observation is more likely the result of a global decrease in the physical sea temperature, as described in the main text.

B.4. Temperature Variations over Ligeia Mare Observed with Beam 3

Of the five beams of the RADAR, beam 3 (the central and circular beam; see Janssen et al. 2016) is the most resolved and best calibrated beam. As another sanity check, we studied the temporal evolution of the temperatures measured with this beam alone (Figure B6). We find a temperature drop of 0.8 ± 0.2 K over the course of the mission, which is slightly larger than when all beams are considered. Averaging the flybys close in time (namely T25/T28/T29 and T91/T92), the decrease is even more pronounced, reaching 1.0 ± 0.2 K.

B.5. Temporal Evolution of Kraken Mare's Effective Temperature

Similarly to Ligeia Mare, the seasonal variation in the temperature of Kraken Mare was investigated. As there is no available bathymetry map for this sea, we set the sea depth at 300 m (the maximum depth Cassini could have probed in the best conditions according to Poggiali 2020). Kraken's effective temperatures were computed as the ratio of the measured brightness temperature and the emissivity (see Section 3 in the

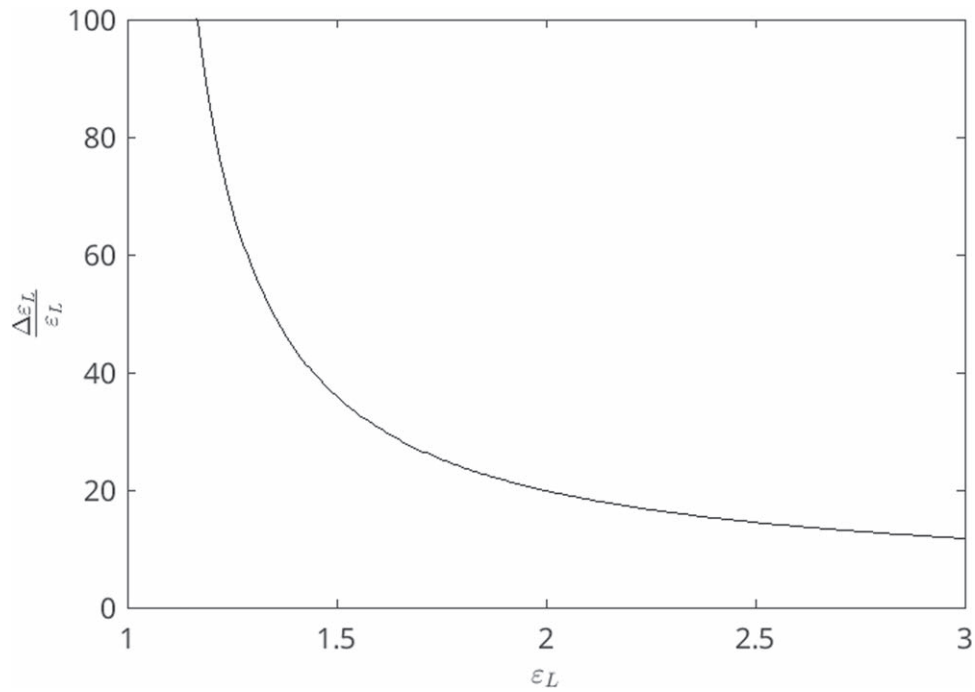


Figure B4. Relative variations in the sea permittivity. To decrease the sea emissivity by 2%, the global sea permittivity has to vary by about 25% in the case of Ligeia Mare ($\epsilon_L = 1.7$).

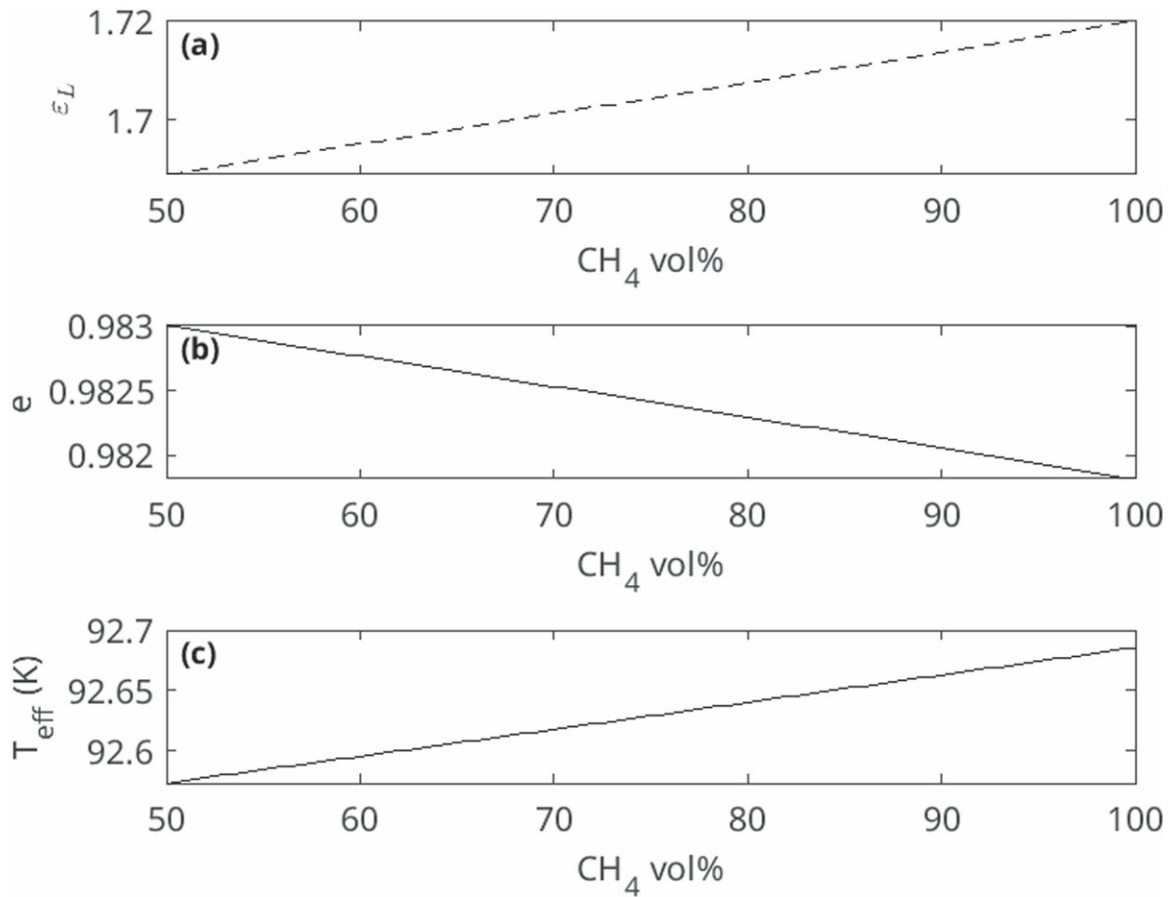


Figure B5. Evolution of the permittivity (a), the emissivity (b), and the derived effective temperature (c) with the concentration of methane in Ligeia Mare.

main paper); they are displayed in Figure B7. Despite the small number of measurements over Kraken Mare and the limited coverage in time, the hint of a decrease in effective

temperature, similar to that observed on Ligeia Mare, can be observed. This suggests that the two polar seas encounter the same or a similar mechanism during boreal spring.

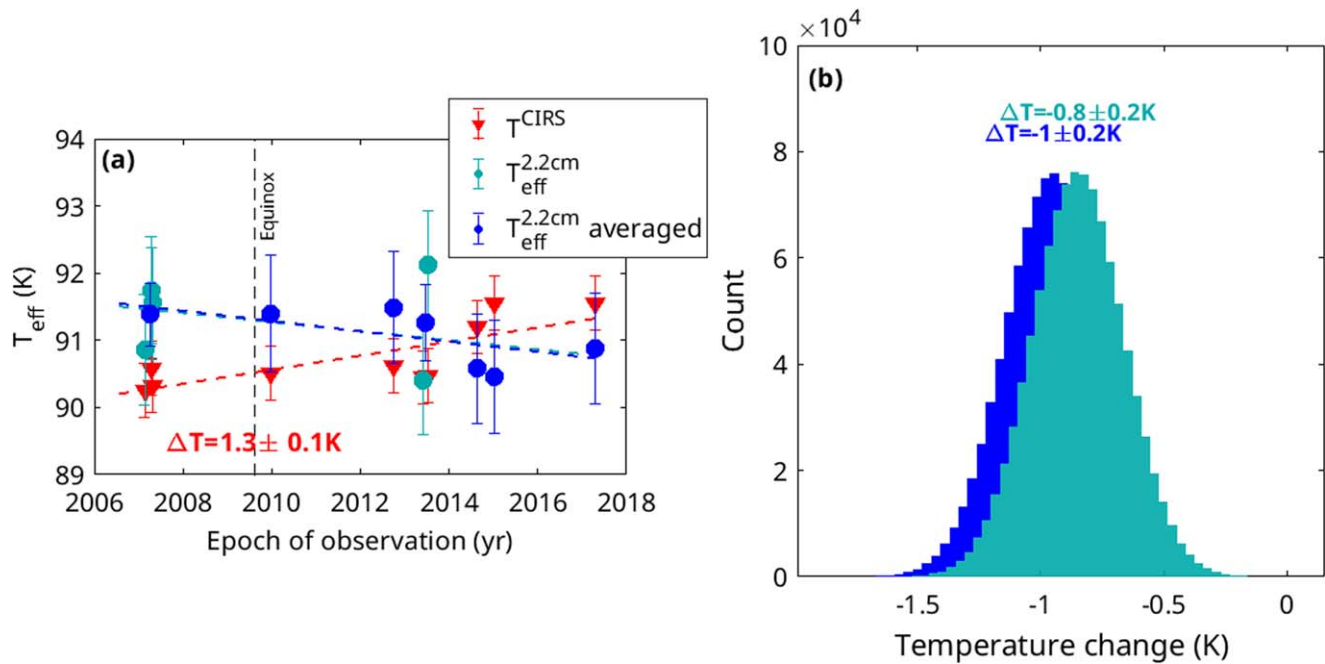


Figure B6. Temporal variations in effective temperature measured on Ligeia Mare, compared to the CIRS-derived surface temperature model prediction (in red) considering beam 3 alone. The blue points differ from the turquoise points as they average the temperatures of T25 T28 and T29 together, and T91 with T92 because of their temporal proximity.

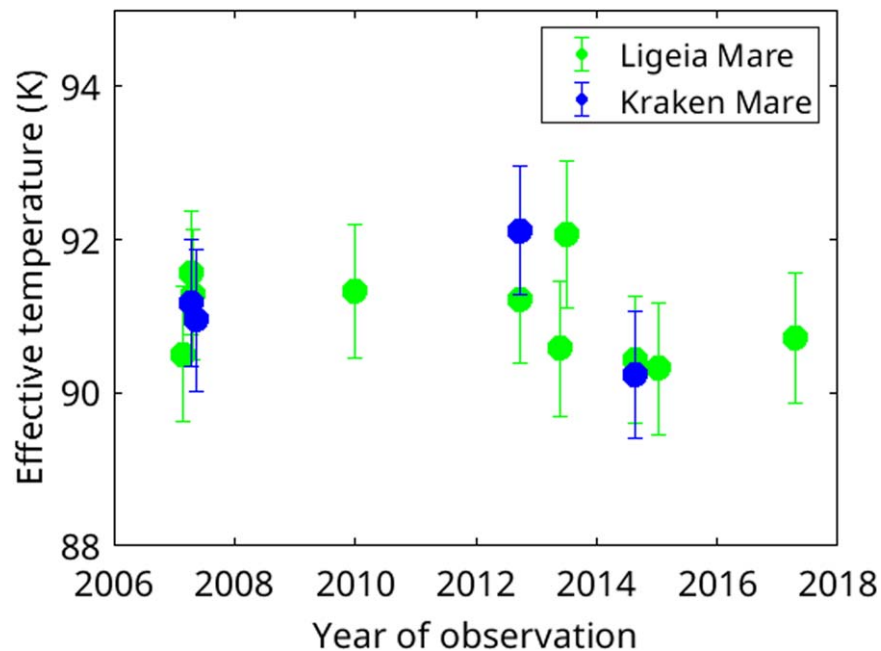


Figure B7. Temporal variations in effective temperature for both Kraken and Ligeia Maria.

ORCID iDs

R. E. Sultana <https://orcid.org/0000-0001-9563-0571>
 T. Tokano <https://orcid.org/0000-0002-7518-9245>
 L. E. Bonnefoy <https://orcid.org/0000-0003-1842-7531>
 R. D. Lorenz <https://orcid.org/0000-0001-8528-4644>

References

- Barnes, J. W., Soderblom, J. M., Brown, R. H., et al. 2011, *Icar*, 211, 722
 Bonnefoy, L. E., Hayes, A. G., Hayne, P. O., et al. 2016, *Icar*, 270, 222
 Bonnefoy, L. E., Le Gall, A., Lellouch, E., et al. 2020, *Icar*, 352, 113947
 Brown, R. H., Baines, K. H., Bellucci, G., et al. 2004, *SSRv*, 115, 111
 Chatain, A., Raffin, S. C. R., Soto, A., Hueso, R., & Spiga, A. 2022, *PSI*, 3, 232
 Cottini, V., Nixon, C. A., Jennings, D. E., et al. 2012, *P&SS*, 60, 62
 Courtin, R., & Kim, S. J. 2002, *P&SS*, 50, 309
 Dhingra, R. D., Barnes, J. W., Brown, R. H., et al. 2019, *GeoRL*, 46, 1205
 Dhingra, R. D., Jennings, D. E., Barnes, J. W., & Cottini, V. 2021, *GeoRL*, 48, e91708
 Elachi, C., Wall, S., Allison, M., et al. 2005, *Sci*, 308, 970
 Flasar, F. M. 1998, *P&SS*, 46, 1125
 Flasar, F. M., Samuelson, R. E., & Conrath, B. J. 1981, *Natur*, 292, 693
 Fulchignoni, M., Ferri, F., Angrilli, F., et al. 2005, *Natur*, 438, 785
 Hayes, A. G. 2016, *AREPS*, 44, 57

- Heiles, C. E., & Drake, F. D. 1963, *Icar*, **2**, 281
- Hofgartner, J. D., Hayes, A. G., Lunine, J. I., et al. 2014, *NatGe*, **7**, 493
- Hofgartner, J. D., Hayes, A. G., Lunine, J. I., et al. 2016, *Icar*, **271**, 338
- Janssen, M. A., Ingersoll, A. P., Allison, M. D., et al. 2013, *Icar*, **226**, 522
- Janssen, M. A., Le Gall, A., Lopes, R. M., et al. 2016, *Icar*, **270**, 443
- Janssen, M. A., Le Gall, A., & Wye, L. C. 2011, *Icar*, **212**, 321
- Janssen, M. A., Lorenz, R. D., West, R., et al. 2009, *Icar*, **200**, 222
- Jennings, D. E., Cottini, V., Nixon, C. A., et al. 2016, *ApJL*, **816**, L17
- Jennings, D. E., Flasar, F. M., Kunde, V. G., et al. 2009, *ApJL*, **691**, L103
- Jennings, D. E., Tokano, T., Cottini, V., et al. 2019, *ApJL*, **877**, L8
- Kuiper, G. P. 1944, *ApJ*, **100**, 378
- Le Gall, A., Leyrat, C., Janssen, M. A., et al. 2014, *Icar*, **241**, 221
- Le Gall, A., Malaska, M. J., Lorenz, R. D., et al. 2016, *JGRE*, **121**, 233
- Le Gall, A., West, R. D., & Bonnefoy, L. E. 2019, *GeoRL*, **46**, 11747
- Le Gall, A. A., Bonnefoy, L. E., Sultana, R., et al. 2023, *Icar*, **394**, 115446
- Lopes, R. M. C., Malaska, M. J., Schoenfeld, A. M., et al. 2020, *NatAs*, **4**, 228
- Lorenz, R. 1999, *Icar*, **142**, 391
- Lorenz, R. D. 2015, *P&SS*, **108**, 66
- Lorenz, R. D., Kraal, E., Asphaug, E., & Thomson, R. E. 2003, *EOSTr*, **84**, 125
- Lorenz, R. D., Lopes, R. M., Paganelli, F., et al. 2008, *P&SS*, **56**, 1132
- Lorenz, R. D., Wall, S., Radebaugh, J., et al. 2006, *Sci*, **312**, 724
- Lunine, J. I., & Atreya, S. K. 2008, *NatGeo*, **1**, 159
- Malaska, M. J., Radebaugh, J., Lopes, R. M. C., et al. 2020, *Icar*, **344**, 113764
- Mastrogiuseppe, M., Hayes, A., Poggiali, V., et al. 2016, *ITGRS*, **54**, 5646
- Mastrogiuseppe, M., Poggiali, V., Hayes, A., et al. 2014, *GeoRL*, **41**, 1432
- McKay, C. P., Pollack, J. B., & Courtin, R. 1991, *Sci*, **253**, 1118
- Mitchell, K. L., Barmatz, M. B., Jamieson, C. S., Lorenz, R. D., & Lunine, J. I. 2015, *GeoRL*, **42**, 1340
- Nixon, C. A., Achterberg, R. K., Adamkovics, M., et al. 2016, *PASP*, **128**, 018007
- Ostro, S. J., West, R. D., Janssen, M. A., et al. 2006, *Icar*, **183**, 479
- Paillou, P., Lunine, J., Ruffié, G., et al. 2008, *GeoRL*, **35**, L18202
- Poggiali, V., Hayes, A. G., Mastrogiuseppe, M., et al. 2020, *JGR*, **125**, e06558
- Rodriguez, S., Vinatier, S., Cordier, D., et al. 2022, *ExA*, **54**, 911
- Schneider, T., Graves, S. D. B., Schaller, E. L., et al. 2012, *Natur*, **481**, 58
- Smith, P. H., Lemmon, M. T., Lorenz, R. D., et al. 1996, *Icar*, **119**, 336
- Sotin, C., Jaumann, R., Buratti, B. J., et al. 2005, *Natur*, **435**, 786
- Stofan, E. R., Elachi, C., Lunine, J. I., et al. 2007, *Natur*, **445**, 61
- Tokano, T. 2005, *Icar*, **173**, 222
- Tokano, T. 2009, *Icar*, **204**, 619
- Tokano, T. 2019, *Icar*, **317**, 337
- Tokano, T., & Lorenz, R. D. 2016, *Icar*, **270**, 67
- Turtle, E. P., Perry, J. E., Barbara, J. M., et al. 2018, *GeoRL*, **45**, 5320
- Ulaby, F., & Long, D. 2015, *Microwave Radar and Radiometric Remote Sensing* (Ann Arbor, MI: Univ. Michigan Press)
- Zebker, H., Hayes, A., Janssen, M., et al. 2014, *GeoRL*, **41**, 308